



Contents lists available at ScienceDirect

NDT and E International

journal homepage: [www.elsevier.com/locate/ndteint](http://www.elsevier.com/locate/ndteint)

Research Paper

## Defect imaging via adjoint-state-based Reverse-time Migration

John D. Day<sup>a</sup>, Jiaze He<sup>a</sup><sup>\*</sup>, Jeffrey Shragge<sup>b</sup>, Paul Sava<sup>b</sup>, Erin L. Lanigan<sup>c</sup>, Gavin Dao<sup>d</sup>, Weihua Su<sup>a</sup><sup>\*</sup>

<sup>a</sup> Department of Aerospace Engineering and Mechanics, The University of Alabama, Tuscaloosa, AL, 35487-0280, United States

<sup>b</sup> Department of Geophysics, Colorado School of Mines, Golden, CO, 80401, United States

<sup>c</sup> NASA Marshall Space Flight Center, Huntsville, AL, 35808, United States

<sup>d</sup> Advanced OEM Solutions, West Chester Township, OH, 45069, United States

### ARTICLE INFO

#### Keywords:

Ultrasound imaging  
Reverse-time Migration  
Adjoint tomography theory  
Nondestructive evaluation

### ABSTRACT

Defects limit the mechanical properties of structural components and can cause failure. Ultrasonic imaging has proven to be an inexpensive and powerful approach to characterize defects and has been of interest in the additive manufacturing sector as quality assurance. Reverse-time migration, a full wavefield imaging approach, provides increased accuracy over a standard Total Focusing Method. Previously reported Reverse-time Migration implementations locate defects without direct relationship to material properties. This motivates an improved approach that prioritizes accuracy in the sizing of defects and reduction in image false-positive amplitudes, denoted as artifacts. This work explores adjoint tomography theory to improve the Reverse-time Migration methodology. The innovation involves several cross-correlation conditions based upon full waveform inversion elastic model parameters (e.g., longitudinal- and shear-wave speed, density, and impedance). It is denoted adjoint-state-based Reverse-time Migration. Two metal specimens with side-drilled holes were inspected using the aforementioned imaging conditions, denoted as kernels. To benchmark the approach, the resulting images were evaluated based on (1) an average background noise analysis and (2) accurate sizing and location of holes. The Total Focusing Method approach is implemented as a benchmark of comparison. The results indicate that the longitudinal wave speed kernel has a consistently superior signal-to-noise ratio. In an example application to numerically generated ultrasound data, the longitudinal wave speed kernel produced an image with a maximum signal-to-noise ratio of 52.36 dB while the Total Focusing Method generated one with 35.65 dB. Practical applications of these findings could be as an in-situ high-accuracy and noise-resistant quality assurance technique for additive manufacturing.

### 1. Introduction

Defect detection is a critical analysis in a wide variety of engineering fields. Routine inspection is performed to detect architectural cracks [1]. Parts must be closely inspected for manufacturing defects before use in a load-bearing assembly [2]. Crack growth is prominent in aerospace structures due to cyclic loading. Routine observation is often required to determine if components need replacement. One function of nondestructive evaluation (NDE) techniques is defect detection, which allows users to predict how soon their part may need to be replaced. In the aerospace sector, wings are inspected for crack growth, which informs when to replace parts based on the observed crack size after cyclical loading in flight [3,4].

Ultrasound imaging (UI) has become a popular NDE approach for defect detection in metals. Common examples are in-situ monitoring

for additive manufacturing and crack detection within aerospace structures [5]. There are benefits to selecting UI for NDE applications over alternatives, such as radiography [6]. For example, UI can penetrate materials that are opaque to electromagnetic waves. UI is enabled by modeling or predicting wave propagation within a region of interest and using ultrasound equipment to send and record ultrasonic waves, which are used to generate an image. The signal processing approach may generate different information about the material, such as the wave speeds, density, and impedance contrasts. Ultrasound signals must be excited so that waves travel from sources, through the inspected domain, and back to receivers. An approach for acquiring ultrasound signals for defect detection is from phased-array transducers, also known as 1-D arrays [7,8]. With this acquisition approach, a standard data format is the full matrix capture (FMC). An FMC consists of each individual source excited once while all other elements

\* Corresponding authors.

E-mail addresses: [jiazehe@gmail.com](mailto:jiazehe@gmail.com) (J. He), [suw@eng.ua.edu](mailto:suw@eng.ua.edu) (W. Su).

<https://doi.org/10.1016/j.ndteint.2025.103425>

Received 23 January 2025; Received in revised form 24 April 2025; Accepted 27 April 2025

Available online 15 May 2025

0963-8695/© 2025 Elsevier Ltd. All rights are reserved, including those for text and data mining, AI training, and similar technologies.

in the array record. This results in a three-dimensional (3-D) dataset indexed by the source, receiver, and time coordinates. These signals are interpreted using UI techniques to characterize defects and differences in material properties.

Ultrasound signals acquired from a physical specimen must be interpreted to provide insight into the domain's characteristics. Synthetic aperture methods are implemented to characterize the orientation and size of imaged defects. Using FMC signals, defect locations can be detected using a known background longitudinal wave speed to measure the elapsed time for waves to travel from a known source location to all points within an imaging domain and then back to a receiver. If the corresponding FMC signal to that source-receiver pair has a nonzero amplitude at that measured time, then a scatterer (e.g., a fracture or hole with contrasting physical properties) is assumed to have been associated with that location. This process is then repeated for each source-receiver pair, and the resulting images are stacked. Depending on which source-receiver combinations are implemented, the method is termed either the Synthetic Aperture Focusing Technique (SAFT) or the Total Focusing Method (TFM) [8–12]. The main difference between the two analyses is that TFM considers all possible source-receiver combinations in the FMC, while SAFT only considers specific combinations. This results in TFM theoretically having an improved signal-to-noise ratio (SNR) [13]. While synthetic aperture methods account for phenomena associated with scattering longitudinal waves, standard TFM does not consider complicated wave phenomena such as multiple scattering, a plurality of wave modes, or potentially complex specimen geometry, which can lead to imaging artifacts [14].

For a more robust imaging method, wave-equation simulators (e.g., finite-element, finite-difference, and spectral-element solvers) mathematically model physical systems over a time window and allow an improved representation of wave phenomena not provided by standard TFM. While this significantly increases computational expenditure, past work has shown that simulator-based techniques generally improve results from imaging with specific benefits depending on the implementation. For example, prior studies demonstrate that Reverse-time Migration (RTM) based on numerical solutions of the acoustic wave equation (i.e., acoustic RTM) provides improved shape accuracy of reconstructed defects over standard TFM [15–18]. However, an obstacle faced by acoustic RTM imaging is the generation of image artifacts caused by impedance contrasts [19] and a failure to accurately represent elastic wave modes [20] resulting in degraded SNR of the entire image.

Numerous RTM imaging conditions have been studied to improve the accuracy of defect characterization [21] and suppress artifacts [19, 20]. Prior studies have indicated that the material property distribution, i.e., longitudinal and shear wave speeds and density, is an important factor when accurately sizing defects [22]. The goal of this study is to propose an improved RTM methodology that uses the elastic adjoint tomography theory (ATT) [23] as the framework for performing RTM-based ultrasound imaging (herein referred to as “ARTM”). The algorithmic basis of ARTM uses a modified backward reconstruction to compute model parameter deviations from a cross-correlation imaging condition [23], which are denoted as “sensitivity kernels”. In seismology, the kernels are a key part of the full waveform inversion (FWI) process, where specific material parameters in the Earth can be characterized by interpreting seismic data. The kernels are indicative of a difference in a targeted material parameter. Their evaluation is similar to applying a standard cross-correlation imaging condition in RTM. This methodology results in images based on deviations of elastic model parameters such as longitudinal and shear wave speeds, or linear combinations thereof (i.e., impedance). The benefit of using the ARTM methodology is that specific imaging conditions may provide a superior image given a certain acquisition geometry compared to the standard RTM imaging condition, as quantified by image SNR and sizing metrics. The rationale for this is that the deviations are attributed to the calculated deviations of material parameters instead of a simple

cross-correlation. This elastic ARTM methodology has been used to successfully highlight reflectivity in the field of seismology [24]; therefore, this work focuses on benchmarking elastic ARTM in an unexplored NDE setting.

This study begins by outlining the classical RTM method based on the acoustic wave equation, RTM's previously reported extensions to the elastic domain, and the integration of ATT with a new RTM methodology (ARTM). Next, the ARTM methodology is benchmarked for defect imaging through numerical tests and practical application to experimental data. In each application, a synthetic aperture method (TFM) is also applied to act as a baseline for comparison. To quantify results, the defect sizes are estimated from the images and compared to known values. In addition, an SNR metric is evaluated to quantify the level of average noise in the image. This method is repeated for four studies. Three of them involve a steel block with side-drilled holes of varying sizes. The steel block studies consist of the following ultrasound data: (1) numerically generated based on the transducer and steel block geometry, (2) acquired from the steel block using a phased-array transducer, and (3) the laboratory data from (2) after contaminating the data to artificially reduce the SNR. The final study applies ARTM to ultrasound data from an aluminum block with holes in the formation “AOS” to demonstrate ARTM's ability to detect and characterize defects partially shadowed or located farther from the transducer aperture.

## 2. Imaging approaches

### 2.1. Acoustic reverse-time migration

A “classical” acoustic RTM process can be described in three parts: (1) forward modeling wavefields  $s(\mathbf{x}_s, \mathbf{x}, t)$  generated by impulsive sources excited at or near the domain boundary at point  $\mathbf{x}_s$  in time interval  $t = [0, T]$  through a numerical specimen model based on known material properties within a defect-free domain  $\mathbf{x} = [x, y]$ , (2) reconstructing a time-reversed adjoint (indicated by  $\dagger$ ) receiver wavefields  $r^\dagger(\mathbf{x}_r, \mathbf{x}, t)$ , by injecting recorded wavefield data in reverse time at each receiver location  $\mathbf{x}_r$ , and (3) applying source-receiver wavefield cross-correlation via an “imaging condition” evaluated at each time step [16,21,25]. In the classical acoustic case, forward and adjoint wavefields are considered scalar pressure disturbances that are simulated throughout the discretized model domain  $\mathbf{x}$ ; however, this approximation necessarily neglects elastic wave phenomena. It is standard to use the acoustic wave equation [26] to model wave propagation and obtain the required components. This may be accomplished by a wave-equation simulator, which iteratively solves the following wave equation for all time  $t$ :

$$\left( \frac{1}{c^2(\mathbf{x})} \frac{\partial^2}{\partial t^2} - \nabla^2 \right) P(\mathbf{x}, t) = \delta(\mathbf{x}_s - \mathbf{x}) f(t), \quad (1)$$

where  $\delta$  represents the Kronecker delta,  $f(t)$  represents the point-source located at  $\mathbf{x}_s$ , and  $P(\mathbf{x}, t)$  represents the scalar pressure wavefield in the domain  $\mathbf{x}$  at time  $t$ . Forward simulations (i.e., on  $t = [0, T]$  s) are used to generate the source wavefields  $s(\mathbf{x}_s, \mathbf{x}, t)$  while adjoint runs (i.e., on  $t = [T, 0]$  s) are used to model the receiver wavefield data  $r^\dagger(\mathbf{x}_r, \mathbf{x}, t)$ . Depending on the robustness simulator being used, spatially heterogeneous material properties may be allowed.

A classical formulation of the imaging condition is a cross-correlation of the acoustic forward source and time-reverse receiver wavefields output from the wave-equation solver [27]. This is represented by the following time integration to generate scalar image  $I_{RTM}$ :

$$I_{RTM}(\mathbf{x}) = \sum_{\mathbf{x}_s} \sum_{\mathbf{x}_r} \int_0^T r^\dagger(\mathbf{x}_r, \mathbf{x}, t) s(\mathbf{x}_s, \mathbf{x}, t) dt, \quad (2)$$

where  $s(\mathbf{x}_s, \mathbf{x}, t)$  corresponds to the numerically generated forward wavefield, which is based on the background (i.e., defect-free) model domain;  $r^\dagger(\mathbf{x}_r, \mathbf{x}, t)$  is the corresponding time-reversed receiver wavefield, which is generated from signals experimentally acquired from

a domain with potential defects; and the summations over  $\mathbf{x}_s$  and  $\mathbf{x}_r$  respectively represent the superposition for all sources and receivers used in the FMC experimental data acquisition. From here onward, the functional dependence of forward wavefields is shortened to  $s(\mathbf{x}, t)$  and adjoint wavefields are shortened to  $r^\dagger(\mathbf{x}, t)$ . It shall be understood that the introduced forces in each of these cases are located at  $\mathbf{x}_s$  and  $\mathbf{x}_r$ , respectively.

Evaluating Eq. (2) generates an image  $I_{RTM}$  that highlights regions with scattering amplitude (i.e., material property discontinuities) within the model domain because the forward source and time-reversed receiver wavefields will be in phase at scatterer boundaries [26,27]. However, an accurate depiction of the scatterer location with RTM depends on wave speed veracity (i.e., longitudinal wave speed); inaccurate longitudinal wave speed models will cause image misfocusing and mispositioning of detected defects.

In the FMC case, the process is repeated for each source shot and ultrasound data associated with it. The result is a composite image representative of the summation expressions in Eq. (2). This helps highlight the defect contour that may be only partially illuminated by a single source position [27].

## 2.2. Elastic Reverse-time migration

One adjustment made to the classical acoustic RTM methodology is implementing elastic wave propagation effects (i.e., longitudinal, shear, and surface waves as well as elastic scattering) and applying some form of an elastic imaging condition. This extension is commonly denoted as elastic RTM (E-RTM) [28].

In acoustic RTM, the waves propagate based on a scalar pressure formulation; however, E-RTM uses a vector displacement or particle velocity formulation [29,30]. An example adaptation of the wave equation from [31] is:

$$\rho \partial_t^2 u_i - \partial_j T_{ij} = f_i, \quad (3)$$

where  $s_i(\mathbf{x}, t)$  is the displacement wavefield. Note that wavefield  $u_i$  in Eq. (3) is expressed in Einstein summation notation where, e.g., an index can be  $i = [x, y, z]$ . From Eq. (3),  $T_{ij}$  is the stress tensor, which may be derived from strain using a linear isotropic constitutive relationship (i.e., Hooke's Law) between the 4th-order elastic stiffness  $c_{ijkl}$  and strain  $\epsilon_{kl}$  tensors:

$$T_{ij} = c_{ijkl} \epsilon_{kl}, \quad (4)$$

where contraction occurs over two tensor indices. To satisfy the free boundary condition, the traction vector must vanish at  $\partial V$ :

$$T_{ij} n_j = 0 \quad \text{on} \quad \partial V, \quad (5)$$

where  $n_i$  is the unit normal vector to a free surface. The initial conditions on wavefield  $u_i$  are met by satisfying:

$$u_i(\mathbf{x}, 0) = 0, \quad \text{and} \quad \partial_t u_i(\mathbf{x}, 0) = 0. \quad (6)$$

Finally, the source  $f_i$  is represented in terms of a moment tensor  $\mathbf{M}$ :

$$f_i = M_{ij} \partial_j \delta(\mathbf{x} - \mathbf{x}_s) f(t), \quad (7)$$

where  $\delta$  is the Dirac delta function, and  $f(t)$  is the source-time function (STF). In seismology, a double-couple source term may be used, which applies both a point force and moment tensor at  $\mathbf{x}_s$ ; however, in this ultrasound NDE study, only a vertically oriented point source term is considered, meaning Eq. (7) may be simplified to

$$f_i = \begin{bmatrix} f_x \\ f_y \\ f_z \end{bmatrix} = \begin{bmatrix} 0 \\ 0 \\ \delta(\mathbf{x} - \mathbf{x}_s) f(t) \end{bmatrix}. \quad (8)$$

Like in the acoustic scenario discussed above, the elastic wave-equation allows one to forward model vector source wavefields  $s_i(\mathbf{x}, t)$  as well as

the time-reversed adjoint vector receiver wavefields  $r_i^\dagger(\mathbf{x}, t)$ . Again, E-RTM can be applied to more general heterogeneous anisotropic media; however, this work specifically targets homogeneous isotropic model domains.

Because of vector displacement wavefield orientations, the classical acoustic cross-correlation imaging condition needs to be modified to handle the vector forward source  $s_i(\mathbf{x}, t)$  and time-reversed adjoint receiver  $r_i^\dagger(\mathbf{x}, t)$  wavefields. Numerous elastic imaging conditions have been proposed. Some implementations consider the scalar representation of the displacement [30] while others apply a modified cross-correlation imaging condition to support vector displacements [29]. Finally, image the energy spatially and temporally coincident in the source and time-reversed receiver wavefields [32]. However, a consistent feature of these E-RTM imaging conditions is that they do not connect the observed imaged features with the underlying model parameter perturbations that give rise to the observed wavefield scattering. ATT aims to fill this gap by connecting the E-RTM imaging conditions to model parameter perturbations.

## 2.3. Adjoint tomography theory

While ATT is relatively unknown for NDE, it has been extensively explored within the seismology community [23,24,33,34]. An aspect of ATT, the sensitivity kernels, has been explored as imaging conditions for a migration process, highlighting specific material property differences and, in some cases, suppressing artifacts [24,34]. This study does not aim to provide a comprehensive explanation of the theory behind ATT, given that it has been previously reported in several seismology papers [e.g.,24,33]; however, the process to derive the sensitivity kernels and their usefulness in NDE is outlined below.

To understand the implementation of ATT, it must be approached from an FWI perspective [31,33]. To start, the agreement of wavefields at recording locations  $\mathbf{x}_r$  must be measured, where  $d_i^M = s_i(\mathbf{x}, t)|_{\mathbf{x}=\mathbf{x}_r}$  are the numerically modeled source wavefields sampled at  $\mathbf{x} = \mathbf{x}_r$ , while  $d_i = d_i(\mathbf{x}_r, t)$  are those recorded experimentally. The least-squares norm is used as a measure of fitness

$$\chi = \frac{1}{2} \sum_{\mathbf{x}_r} \int_0^T (d_i^M - d_i)^2 dt. \quad (9)$$

The minimization of the action is achieved by reducing the misfit in Eq. (9) while satisfying Eq. (3)

$$\chi = \frac{1}{2} \sum_{\mathbf{x}_r} \int_0^T \left( (d_i^M - d_i)^2 dt - \int_V \lambda_i (\rho \partial_t^2 s_i - \partial_j T_{ij} - f_i) d^3 x_i \right) dt, \quad (10)$$

where  $\lambda_i(\mathbf{x}, t)$  is the Lagrange multiplier. Following [31], the variation of the action is taken after a few algebraic adjustments to Eq. (10). The first is implementing the isotropic constitutive relationship Eq. (4) to uncover the elastic tensor. Here, the variation is represented by the symbol  $\delta$  next to a physical field (e.g.,  $\delta s_i(\mathbf{x}, t)$ ), and should not be confused when it is implemented as the Dirac delta applied to a physical coordinate (i.e.,  $\delta(\mathbf{x} - \mathbf{x}_r)$ ). After, several terms are integrated, involving spatial and temporal derivatives of both  $s_i$  and  $\delta s_i$  by parts. In addition, the boundary condition, Eq. (5), and initial conditions, Eq. (6), are also perturbed. The result of this is a modified version of Eq. (10) as

$$\delta \chi_1 = (d_i^M - d_i) \delta(\mathbf{x} - \mathbf{x}_r) \delta s_i, \quad (11)$$

$$\delta \chi_2 = \delta \rho \lambda_i \partial_t^2 s_i + (\partial_i \lambda_j) \delta c_{ijkl} (\partial_k s_l) - \lambda_i \delta f_i, \quad (12)$$

$$\delta \chi_3 = -[\rho \partial_t^2 \lambda_i - \partial_j (c_{ijkl} \partial_k \lambda_l)] \delta s_i, \quad (13)$$

$$\delta \chi_4 = -n_i c_{ijkl} (\partial_j \lambda_k) \delta s_l, \quad (14)$$

$$\delta \chi_5 = -\rho [\lambda_i \partial_t \delta s_i - (\partial_t \lambda_i) \delta s_i], \quad (15)$$

where

$$\delta \chi = \frac{1}{2} \sum_{\mathbf{x}_r} \int_V \left[ \int_0^T (\delta \chi_1 + \delta \chi_2 + \delta \chi_3 + \delta \chi_4) dt + [\delta \chi_5]_T \right] dx_i^3, \quad (16)$$

where the notation  $[\cdot]_T$  indicates that the bracketed function is evaluated at the end time  $T$ . Following [31], if the variation in model parameters is disregarded (i.e.,  $\delta\rho = \delta c_{ijkl} = \delta f_i = 0$ ), the variation of action is stationary in Eq. (16) with respect to perturbations in displacement  $\delta s_i$ , as long as the Lagrange multiplier  $\lambda_i(\mathbf{x}, t)$  satisfies

$$\rho \partial_{tt}^2 \lambda_i - \partial_j (c_{ijkl} \partial_k \lambda_l) = \sum_{\mathbf{x}_r} (d_i^M - d_i) \delta(\mathbf{x} - \mathbf{x}_r). \quad (17)$$

The other terms in Eq. (16) are the boundary condition (Eq. (14))

$$\delta \chi_4 = 0 \quad \text{on } \partial V, \quad (18)$$

and end of time conditions (Eq. (15))

$$\lambda_i(\mathbf{x}, T) = 0 \quad \text{and} \quad \partial_t \lambda_i(\mathbf{x}, T) = 0, \quad (19)$$

which allows Eq. (16) to be further simplified to

$$\delta \chi = - \int_0^T \int_V [\delta \rho \lambda_i \partial_{tt}^2 s_i + (\partial_t \lambda_j) \delta c_{ijkl} (\partial_k s_l) - \lambda_i \delta f_i] d^3 x_i dt, \quad (20)$$

which is a direct relationship between the perturbed model parameters and the changes in the misfit function as well as the numerically modeled forward wavefields  $s_i$ , which are evaluated by a wave equation simulator, and the Lagrange multiplier as a wavefield  $\lambda_i$ .

### 2.3.1. Adjoint wavefields and sources

The adjoint wavefield is defined as

$$r_i^\dagger(\mathbf{x}, t) \equiv \lambda_i(\mathbf{x}, T - t). \quad (21)$$

It is apparent that  $r_i^\dagger$  is the time-reversed version of the Lagrange wavefield. Replacing  $\lambda_i$  with  $r_i^\dagger$ , the following equations are redefined

$$\rho \partial_{tt}^2 r_i^\dagger - \partial_j T_{ij}^\dagger = \sum_{\mathbf{x}_r} (d_i^M(\mathbf{x}_r, T - t) - d_i(\mathbf{x}_r, T - t)) \delta(\mathbf{x} - \mathbf{x}_r), \quad (22)$$

where  $T_{ij}^\dagger$  is the adjoint stress. It is related to the adjoint wavefield by

$$T_{ij}^\dagger = c_{ijkl} \partial_k s_l^\dagger. \quad (23)$$

The adjoint wave equation, Eq. (22), is subjected to the free-surface boundary condition

$$n_j T_{ij}^\dagger = 0 \quad \text{on } \partial V, \quad (24)$$

as well as the initial conditions

$$r_i^\dagger(\mathbf{x}, 0) = 0 \quad \text{and} \quad \partial_t r_i^\dagger(\mathbf{x}, 0) = 0. \quad (25)$$

It is apparent that the forward wavefield  $s_i$  and adjoint wavefield  $r_i^\dagger$  are governed by the same wave equation with an exception. While  $s_i$  is influenced by the source term  $f_i$ ,  $r_i^\dagger$  is influenced by the time-reversed differences (i.e., ‘‘residuals’’) between the forward modeled wavefields and experimental signals in Eq. (22), which are the adjoint sources

$$f_i^\dagger = (d_i^M(\mathbf{x}_r, T - t) - d_i(\mathbf{x}_r, T - t)) \delta(\mathbf{x} - \mathbf{x}_r). \quad (26)$$

Tromp et al. [31] discussed that post-processing usually occurs when forming adjoint sources; this will also be the case in the ARTM framework. The post-processing implemented to form the adjoint sources will be discussed later within Section 3.6.

### 2.3.2. Sensitivity kernels

Continuing with [33], Eq. (20) is further refined using the adjoint wavefield definition and the following substitutions  $\delta \ln \rho = \delta \rho / \rho$  and  $\delta \ln c_{ijkl} = \delta c_{ijkl} / c_{ijkl}$  (interpreted element-by-element)

$$\delta \chi = \int_V \left[ (\delta \ln \rho K_\rho + \delta \ln c_{ijkl} K_{ijkl}) + \int_0^T r_i^\dagger \delta f_i dt \right] d^3 x_i. \quad (27)$$

The two new terms, scalar  $K_\rho$  and tensor  $K_{ijkl}$ , are the finite-frequency sensitivity kernels with respect to density and the 4th-order stiffness tensor. The deviation in the source is not of interest within this particular study, although it is a key component of the FWI process.

For this study, only the perturbation of material properties will be considered [33]

$$\delta \chi = \int_V [\delta \ln \rho K_\rho + \delta \ln c_{ijkl} K_{ijkl}] d^3 x_i. \quad (28)$$

These kernels are assembled from the forward and adjoint wavefield terms as well as the deviation in the  $\delta \rho$  and  $\delta c_{ijkl}$  model parameters, i.e.,

$$K_\rho(\mathbf{x}) = -\rho \int_0^T r_i^\dagger \partial_{tt}^2 s_i dt, \quad (29)$$

and

$$K_{ijkl}(\mathbf{x}) = - \int_0^T \partial_t r_j^\dagger \partial_k s_l dt. \quad (30)$$

The two kernels are analogous to imaging conditions for RTM, as they involve a cross-correlation of a forward wavefield and a corresponding time-reversed adjoint wavefield to locate a deviation in material parameters. In this paper,  $K_\rho$  is implemented during each study, and  $K_{ijkl}$  is further refined and not implemented in tensorial form.

To modify  $K_{ijkl}$ , an isotropic material assumption is made based on the following constitutive relationship

$$c_{ijkl} = (\kappa - 2\mu/3) \delta_{ij} \delta_{kl} + \mu(\delta_k \delta_{jl} + \delta_{il} \delta_{jk}), \quad (31)$$

where  $\kappa$  and  $\mu$  are the bulk and shear modulus, respectively. This expression is first used to replace the tensorial sensitivity kernel  $K_{ijkl}$  in Eq. (28) with two scalar sensitivity kernels for  $\kappa$  and  $\mu$ ,  $K_\kappa = K_\kappa(\mathbf{x})$  and  $K_\mu = K_\mu(\mathbf{x})$ , respectively

$$\delta \chi = \int_V [K_\rho \delta \ln \rho + K_\mu \delta \ln \mu + K_\kappa \delta \ln \kappa] d^3 x_i, \quad (32)$$

where the model parameter substitution,  $\delta \ln \kappa = \delta \kappa / \kappa$  and  $\delta \ln \mu = \delta \mu / \mu$ , are given by

$$K_\kappa = -\kappa \int_0^T \partial_t \delta r_i^\dagger \partial_j s_j dt, \quad (33)$$

and

$$K_\mu = -2\mu \int_0^T D_{ij}^\dagger D_{ij} dt, \quad (34)$$

where

$$D_{ij} = \frac{1}{2} [\partial_t s_j + \partial_j s_i] - \frac{\delta_{ij}}{3} \partial_k s_k, \quad (35)$$

and

$$D_{ij}^\dagger = \frac{1}{2} [\partial_t \delta r_j^\dagger + \partial_j \delta r_i^\dagger] - \frac{\delta_{ij}}{3} \partial_k \delta r_k^\dagger, \quad (36)$$

are the traceless strain deviator and its corresponding adjoint, respectively, and  $\delta_{ij}$  is the Kronecker delta function [24]. Weighted combinations of Eqs. (33) and (34) lead to expressions for longitudinal  $V_p$  and shear  $V_s$  wave speed kernels

$$K_{V_p} = 2(1 + 4\mu/3\kappa) K_\kappa, \quad (37)$$

$$K_{V_s} = 2(K_\mu - (4\mu/3\kappa) K_\kappa). \quad (38)$$

These two kernels with respect to wave speed are a map of the wave speed variation in a domain of interest. For NDE purposes, it will highlight regions that deviate with respect to each parameter. Finally, to encapsulate the effects of all variations in a model, an alternative density kernel  $K_\rho'$  [23] can be computed by

$$K_\rho' = K_\rho + K_\kappa + K_\mu. \quad (39)$$

The kernel is also named the impedance kernel [24] due to its equivalence with longitudinal- and shear-wave impedance. The impedance kernel provided the optimal image due to the canceling of large-scale artifacts from individual kernels used in its evaluation [24].

From a theoretical perspective, the difference between each of these images is the specific material property deviation they represent. For

FWI implementations, specific kernels are implemented to iteratively refine an estimate of a specific parameter. When implemented in an ARTM scheme, they only characterize the deviation, as the exact material properties are not required for sizing and location. In prior geophysics-based ARTM implementations, the purpose was determining the locations and borders of reflectors in the Earth [23]. This is similar to NDE goals: determining locations of scatterers in a structure with known material properties.

#### 2.4. Total focusing method

This study uses a standard TFM [10] as a baseline to compare with ARTM regarding defect imaging in the steel specimen. Both methodologies consider all source-receiver combinations within the FMC, which leads to relevant comparisons. Previous studies demonstrate that classical acoustic RTM has advantages in accuracy and shape reconstruction over standard TFM [1,17,35].

The TFM algorithm uses signals for each source-receiver pair in an FMC, where  $N_s$  and  $N_r$  are the total number of sources and receivers, respectively. The imaging domain may be represented as 1-D components of pixel locations  $\mathbf{x} = [x, z]$  forming a two-dimensional (2-D) image  $I_{TFM}(\mathbf{x})$ . Physical image positions of a particular source in the FMC may be represented as the points  $\mathbf{x}_s$  while for a particular receiver may be represented as  $\mathbf{x}_r$ . The distance from the source  $\mathbf{x}_s$  to all pixels within the 2-D imaging domain  $\mathbf{x}$  may be represented by a 2-D matrix  $D_s(\mathbf{x}_s, \mathbf{x})$  the same size as the final image. Likewise, for a receiver  $\mathbf{x}_r$  this distance to all pixels in the image  $\mathbf{x}$  may be represented by  $D_r(\mathbf{x}, \mathbf{x}_r)$ . These tables were evaluated using Eq. (40) in terms of the Euclidean distance metric,  $\|p\| = \sqrt{p_i p_i}$ :

$$D_s(\mathbf{x}_s, \mathbf{x}) = \|\mathbf{x}_s - \mathbf{x}\| \quad \text{and} \quad D_r(\mathbf{x}, \mathbf{x}_r) = \|\mathbf{x} - \mathbf{x}_r\|. \quad (40)$$

When divided by the longitudinal wave speed, these distances represent the elapsed two-way travel time  $\mathcal{T}(\mathbf{x}_s, \mathbf{x}, \mathbf{x}_r)$  for a longitudinal wave to travel from source  $\mathbf{x}_s$  to a scatterer within  $\mathbf{x}$  and back to receiver  $\mathbf{x}_r$ .

$$\mathcal{T}(\mathbf{x}_s, \mathbf{x}, \mathbf{x}_r) = \frac{D_s(\mathbf{x}_s, \mathbf{x}) + D_r(\mathbf{x}, \mathbf{x}_r)}{V_p}, \quad (41)$$

where  $V_p$  is a homogeneous background longitudinal wave speed.

Eq. (41) effectively models a 2-D space filled with travel times from  $\mathbf{x}_s$  to each pixel and back  $\mathbf{x}_r$ . The 3-D data cube of signals for the corresponding source and receiver data volume for an FMC is referred to as  $S(\mathbf{x}_s, \mathbf{x}_r, \mathcal{T})$ . For each pixel in the domain, the signals may be referenced, assigning a magnitude to each pixel based on  $\mathcal{T}$ . Repeating this action across all source and receiver combinations for the domain  $\mathbf{x}$  generates a 2-D image  $I_{TFM}(\mathbf{x})$ ,

$$I_{TFM}(\mathbf{x}) = \sum_{\mathbf{x}_s} \sum_{\mathbf{x}_r} S(\mathbf{x}_s, \mathbf{x}_r, t) \Big|_{t=\mathcal{T}(\mathbf{x}_s, \mathbf{x}, \mathbf{x}_r)}, \quad (42)$$

where the double summation of  $\mathbf{x}_s$  and  $\mathbf{x}_r$  is over all FMC source and receiver positions.

### 3. Methodology

The ARTM process is applied to three different domains to benchmark the algorithm's performance: (1) numerically generated signals from a synthetic model of the steel block with holes, (2) experimental signals obtained from the real steel block with holes, and (3) experimental signals obtained from the aluminum block with holes. This section introduces the specimens being examined, describes the data acquisition parameters, and outlines key computational details.

**Table 1**  
Specimen dimensions and assumed physical properties.

| Specimen inspected            | Steel | Aluminum |
|-------------------------------|-------|----------|
| Length (mm)                   | 154.8 | 300.0    |
| Width (mm)                    | 31.8  | 20.0     |
| Height (mm)                   | 31.8  | 300.0    |
| $E$ (GPa)                     | 205   | 68.9     |
| $\nu$                         | 0.29  | 0.33     |
| $\rho$ ( $\text{Mg m}^{-3}$ ) | 7.85  | 2.7      |
| $V_p$ ( $\text{km s}^{-1}$ )  | 5.89  | 6.15     |
| $V_s$ ( $\text{km s}^{-1}$ )  | 3.20  | 3.10     |
| $\lambda_f$ (mm)              | 1.18  | 2.05     |
| $\lambda_s$ (mm)              | 0.64  | 1.03     |

**Table 2**  
Steel block hole dimensions and positions.

| Hole number:                            | 1               | 2               | 3               | 4               | 5               | 6               |
|---|-----------------|-----------------|-----------------|-----------------|-----------------|-----------------|
| Distance from left side to center (mm)  | 45.6            | 61.9            | 74.3            | 85.8            | 96.5            | 106.7           |
| Distance from surface to hole edge (mm) | 13.3            | 14.3            | 14.9            | 15.3            | 15.5            | 15.7            |
| Hole diameter (mm)                      | 5.2             | 3.2             | 2.0             | 1.2             | 0.8             | 0.4             |
| Hole diameter in wavelengths            | $8.13\lambda_s$ | $5.00\lambda_s$ | $3.13\lambda_s$ | $1.89\lambda_s$ | $1.25\lambda_s$ | $0.63\lambda_s$ |

#### 3.1. Data acquisition and specimen description

Two specimens were examined in this study. The first specimen is a steel block with multiple side-drilled holes that decrease in size, presented in Fig. 1(a). Applying ARTM-enabled ultrasound NDE to this specimen allows an analysis of algorithmic performance to identify defect sizing and position. The second specimen is shown in Fig. 1(b). It contains side-drilled holes in the formation of "AOS". The ARTM-based NDE of this specimen allows an analysis of the algorithm's performance in sizing holes further from the transducer aperture and partially occluded from the surface. The geometries and estimated material properties of the two specimens are outlined in tabular format. Regarding the steel block, the dimensions are outlined in Table 1 while the hole geometries and positions are described within Table 2. These geometries were obtained by measuring the specimen with calipers, which allowed the hole positions and diameters to be characterized within  $\pm 0.1$  mm. For the aluminum block, the geometry is outlined in Table 1. The aluminum block's whole domain is not of interest in this application. The holes that are being examined are known to be within a  $100 \text{ mm} \times 60 \text{ mm}$  region underneath the transducer. The hole positions can be correlated using the image presented in Fig. 2(b). Their approximate size is also estimated to be 1 mm in diameter. When compared to the estimated wavelength in Table 1, the holes are approximately  $\lambda_s$  in size.

The estimated longitudinal wave speed ( $V_p$ ) and shear wave speed ( $V_s$ ) for the aluminum and steel blocks are evaluated using the following equations

$$V_p = \sqrt{\frac{E(1-\nu)}{\rho(1+\nu)(1-2\nu)}} \quad \text{and} \quad V_s = \sqrt{\frac{E}{2\rho(1+\nu)}}, \quad (43)$$

and the material properties presented in and presented in Table 1 [36].

The ultrasound data acquisition was performed at Advanced OEM Solutions (AOS) using the Pioneer 128/128 FMC & PAUT Instrument. Both specimens had ultrasound signals acquired from their domain with linear phased-array transducers. The transducer is in contact with the top surface of the specimens, as depicted in Figs. 2(a) and 2(b). Note that the aluminum block dataset (Fig. 2(b)) contains two "dead" elements that are neglected in ARTM and TFM applications. Ultrasound couplant is placed between the surface of the block and the transducer. The transducers each operate under the format of an FMC in reflective mode, producing a table of signals equivalent to a  $128 \times 128 \times 1500$  data cube. The first dimension is associated with each source excitation, while the second corresponds to each receiver, and the third is time.

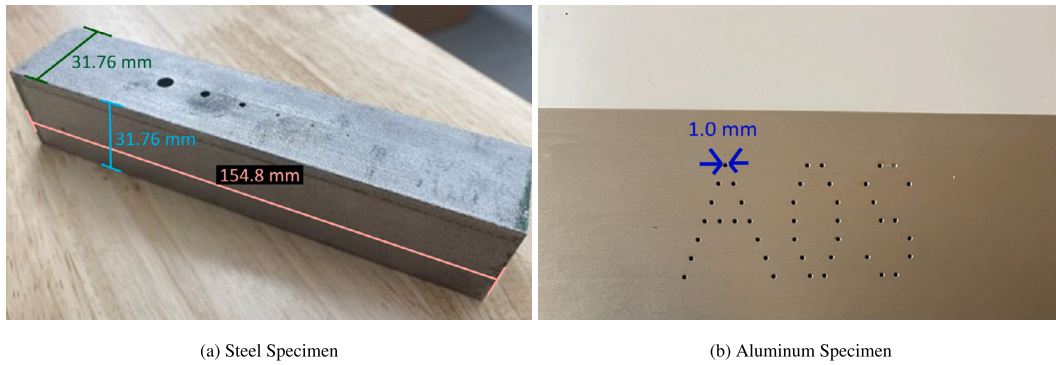


Fig. 1. (a) Steel block with decreasing hole size. (b) Aluminum block with “AOS” hole pattern.

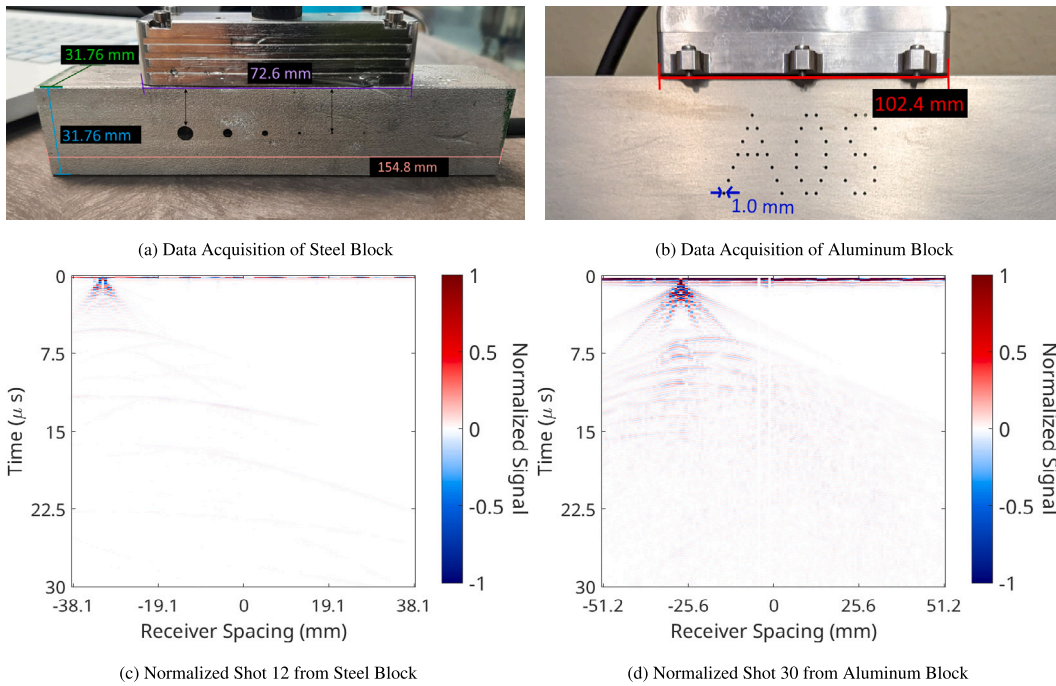


Fig. 2. Data acquisition for steel (a) and aluminum (b) blocks. Shots in the FMC for steel (c) and aluminum (d) datasets.

This expression is equivalent to the  $d_z(x_r, t)$  mentioned in Section 2.3.1. Since the transducers were placed by hand in contact with the surface, the repeatability of generating this exact dataset is not guaranteed; however, if the transducers were placed in the same region as during this study, the same defects would be presented in the final image. If higher precision is required, such transducers can also be implemented using mechanical arms, which can provide improved accuracy for source placement if an application requires it. A large number of sources induces a large computational burden on ARTM, as forward and adjoint simulations are required for each source excitation. If the number of transducers were to be lowered, the authors predict that the quality of the method would falter similarly to that of TFM. To limit the scope of this study, the number of transducers in the acquisition remains constant. A future study could benchmark the method with TFM for imaging with fewer transducers.

### 3.2. Solver environment

The ARTM process incorporated the open-source spectral-element solver SPECFEM2D [31,37], published under the GPL3 license, and the Python framework SeisFlows. The frameworks functioned in tandem to generate forward wavefields  $s_i(x, t)$ , adjoint wavefields  $r_i^\dagger(x, t)$ , and kernels  $K_p, K_{V_p}, K_{V_s}$ , and  $K'_p$ .

#### 3.2.1. Overview of SPECFEM2D

SPECFEM2D serves as the wave-equation solver to generate (1) forward wavefields, (2) wavefields, and (3) kernels for density, longitudinal and shear wave speeds, and impedance with Eqs. (29), (37) and (39). With several kernels, they may be evaluated to determine which produces the best image for NDE of side-drilled holes with the best SNR. SPECFEM2D is a spectral-element solver based on the Galerkin approach. It is widely implemented within seismology studies yet has seen significantly less exploration within the NDE community. It is compatible with parallel computing and graphical processing units (GPUs) and can even model coupled acoustic-elastic domains. When modeling wave propagation in SPECFEM2D, two conditions are maintained. First, mesh coarseness is dictated by the number of points per wavelength, which is advised to be greater than 5.5 for longitudinal wavelengths (i.e.,  $\lambda_l$ ) in acoustic material and 4.5 per shear wavelength (i.e.,  $\lambda_s$ ) in elastic material. These mesh density criteria are advised by the SPECFEM2D manual. Using a mesh density of less than the suggested values will result in inaccuracies in the wavefield calculations, while using more will result in very good accuracy and will take longer to compute wavefields. From [38], it is concluded from their study of the elastic spectral element method that 4.5 points per wavelength are required to limit the effects of numerical dispersion. An aspect to

**Table 3**  
Linear phased-array transducer properties.

| Specimen inspected          | Steel | Aluminum |
|-----------------------------|-------|----------|
| Number of elements          | 128   | 128      |
| Pitch (mm)                  | 0.6   | 0.8      |
| Aperture (mm)               | 72.6  | 102.4    |
| Frequency (MHz)             | 5     | 3        |
| Sampling rate (MHz)         | 50.0  | 50.0     |
| Time step length (ns)       | 20    | 20       |
| Total time steps            | 1500  | 1500     |
| Acquisition time ( $\mu$ s) | 30.0  | 30.0     |

note is that each spectral element has four associated Gauss–Lobatto–Legendre (GLL) points. The final images and wavefields generated by SPECSEM2D have 4x the number of pixels in each direction when four GLL points are implemented [31]. Another requirement that should be considered is the Nyquist sampling theorem, which states that to accurately reconstruct the solutions to the wavefield in a domain, the grid sizing is at most double the desired resolution in each direction. This will be reiterated when discussing the mesh sizes for each study. A Courant–Friedrichs–Lewy (CFL) stability condition is recommended to be kept below 0.5 and must remain below 1.0, limiting the allowable simulation time step size. The 2-D Courant number,  $C$ , is evaluated as

$$C = dt V_p \left( \frac{1}{dx} + \frac{1}{dz} \right) < 0.5, \quad (44)$$

where  $dx$  and  $dz$  are the element sizes in  $X$  and  $Z$  respectively and  $dt$  is the time step length. For the overall simulation stability, Eq. (44) is evaluated at the minimum grid size and largest longitudinal wave speed. These criteria are automatically calculated within the solver and displayed to the user. SPECSEM2D is capable of simulating wave propagation in both heterogeneous and homogeneous backgrounds; however, in this study, the background is assumed to be homogeneous. SPECSEM2D currently supports both isotropic and anisotropic wave modeling; more information may be found within [31].

### 3.2.2. Overview of SeisFlows

Because 128 source excitations occur in each case, a framework was implemented to simultaneously perform wavefield simulations for individual sources, as manually interacting with SPECSEM2D for each source excitation would be cumbersome. The Python-based SeisFlows inversion framework [39,40] was implemented to accomplish this by launching several instances of SPECSEM2D in a parallel MPI format. Normally, SeisFlows is implemented to carry out the FWI methodology, which involves the evaluation of the sensitivity kernels. Because ARTM is not a full waveform inversion method, it is stopped after the first kernel evaluation. A future study could potentially explore the use of the SeisFlows FWI framework to iteratively improve images.

### 3.3. Mesh and simulation parameters

SPECSEM2D was implemented to generate both forward and adjoint wavefields,  $s_i(\mathbf{x}, t)$  and  $r_i^\dagger(\mathbf{x}, t)$ , required for generating ARTM images using the kernel equations outlined in Section 2.3.2. The mesh sizes are compliant with the number of points per wavelength restrictions. In this study, three different simulations were devised, two for defect-free models of steel and aluminum blocks, and a final one for the defect-containing steel block for numerical data generation. Table 4 outlines the parameters for each simulation. For the steel and aluminum blocks, the internal mesher packaged with SPECSEM2D was used to build the mesh out of rectangular elements with material characteristics consistent with the wave speed and density estimates outlined in Table 1. The mesh size is slightly larger in length than the scanning region. This is because three elements on the left, right, and bottom of the domains are designated as the perfectly matched layer (PML) [41,42]. Absorbing boundary conditions are implemented because the true edge

**Table 4**  
Simulation and mesh parameters.

| Simulation                | Steel | Defected Steel | Aluminum |
|---------------------------|-------|----------------|----------|
| Length, $X$ (mm)          | 80.0  | 154.8          | 110.0    |
| Height, $Z$ (mm)          | 31.8  | 31.8           | 60.0     |
| Elements in $X$           | 400   | –              | 300      |
| Elements in $Z$           | 160   | –              | 180      |
| Element size ( $X$ ) (mm) | 0.200 | –              | 0.366    |
| Element size ( $Z$ ) (mm) | 0.199 | –              | 0.333    |
| Points per $\lambda_s$    | 4.795 | 4.67           | 5.06     |
| $dt$ (nm)                 | 2.5   | 0.48           | 4.0      |
| $N_T$                     | 6000  | 31 250         | 7500     |
| $T$ ( $\mu$ s)            | 15    | 15             | 30       |
| Courant Number            | 0.43  | 0.49           | 0.43     |

of the domain is often significantly further than the edges described in the simulation and ultrasound signal. PML allows a reduction in mesh size and improved computational efficiency.

The sizing of the elements in the domain is constrained by two aspects: (1) the Nyquist spatial frequency and (2) the suggested 4.5 points per  $\lambda_s$ . The pixel sizes must be small enough to detect a defect of size  $n$ . The Nyquist theorem requires that the element size should be no greater than  $n/2$ . The smallest defect size within the steel block is a 0.4 mm diameter circle, meaning that the size of elements in the steel block model should be at most 0.2 mm  $\times$  0.2 mm. As indicated in Table 4, the size of the element satisfies this requirement for the steel block model. Specifically, the size of an element in both  $X$  and  $Z$  is less than or equal to 0.2 mm. In addition, the number of points per  $\lambda_s$  must be greater than 4.5; this information is presented when the model is implemented in SPECSEM2D. As indicated in Table 4, this requirement is satisfied for the steel block model. The model used in the aluminum block study must also satisfy the element sizing requirements. The defect size in the aluminum block is 1.0 mm diameter, meaning the mesh must have a resolution of at most 0.5 mm  $\times$  0.5 mm. Referring to Table 4 reveals that the resolution requirements are satisfied, as the size of an element is 0.366 mm by 0.333 mm. In Table 4, the requirement of 4.5 point per  $\lambda_s$  is satisfied based upon the value presented in SPECSEM2D when modeling the aluminum block. Regarding the numerical defected model, it would be cumbersome to define regions where the circular holes would be using SPECSEM2D's internal mesher interface. Instead, an external program was utilized to generate the mesh.

### 3.4. Numerical data acquisition of steel block

SPECSEM2D allows the usage of an externally generated mesh in its framework, which in this study is from Gmsh. This mesh satisfies the hole geometries described in Table 2. The material properties for steel are kept consistent with the estimated properties outlined in Table 1. The acquisition geometry is tailored to match the experimental data acquisition. Sources and receivers are inserted into the top of the domain representing an FMC in the domain that mimics the properties of the 5 MHz transducer shown in Table 3 as well as the location shown in Fig. 2(a). The result is the model depicted in Fig. 3. The STF used when simulating wave propagation is in the format of a 5 MHz center frequency Ricker wavelet; this matches the source frequency of the physical transducer and creates a small few peaks in the numerically generated signals. Another difference between the numerically modeled and the experimental ultrasound data is the number of time steps  $N_T$  and the sampling rate  $f_s$ , depicted in Table 4. The reason why this numerical model requires a much finer temporal sampling scheme is to satisfy the CFL stability criterion. Elements surrounding the smallest hole (shown in Fig. 3) are very small, impacting the Courant number. With these properties, signals equivalent to a 128  $\times$  128  $\times$  31250 data cube are generated as  $d_i(\mathbf{x}_s, \mathbf{x}_r, t)$  representing ultrasound signals obtained from the steel block.

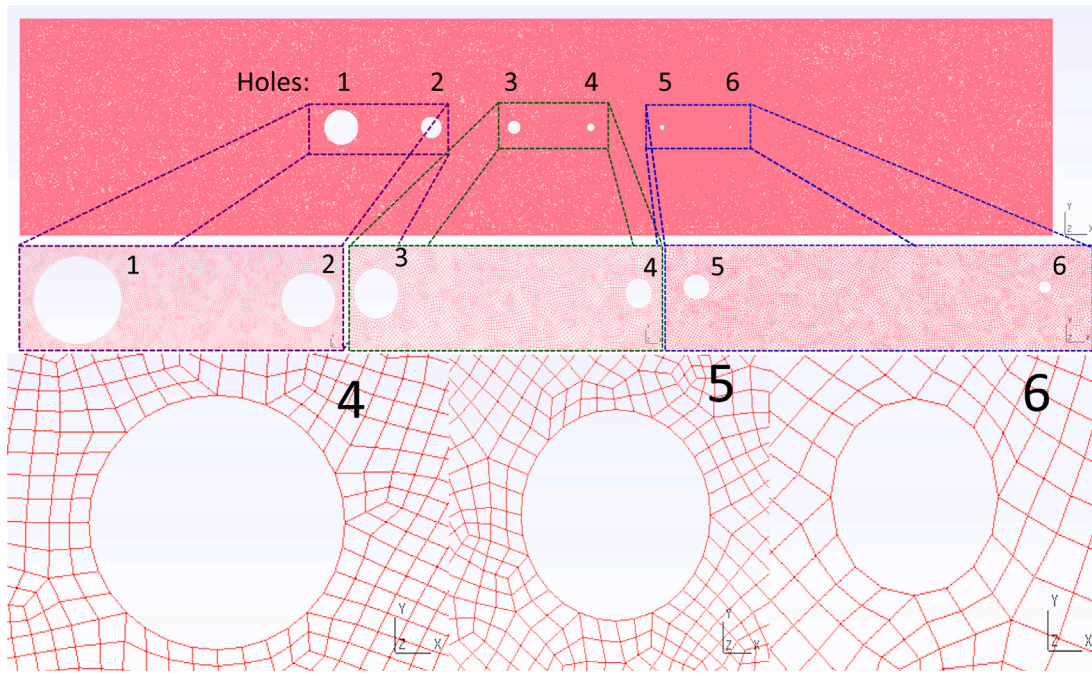


Fig. 3. Externally generated mesh in Gmsh application.

### 3.5. Image quality analysis

Image quality will be determined by examining the hole sizes and locations in the ARTM- and TFM-generated images in comparison to the known values. Characterizing hole edges is required to estimate an accurate hole size, and in certain cases where the background noise is too high, it may be too difficult to discern the defect characteristics. In this study, the defect sizes will be determined with the assistance of an SNR metric using the following whole-image expression [43]

$$SNR = 20 \log_{10} \left( \frac{|I|_{max}}{|I|_{Mean}} \right), \quad (45)$$

where  $|I|_{max}$  represents the peak signal of a defect, and  $|I|_{Mean}$  represents the mean noise value within the image, found by taking the mean value of the signals within the image without the known defects. For the steel block, the noise is derived from the region between  $z = [-8, 8]$  mm within the image, while for the aluminum block images, the analysis will consider the full image without defects. For analysis of holes in the steel block, the local region near the expected defect will be presented, ranging from 8 mm × 8 mm to 4 mm × 4 mm centered on the expected defect location with the region becoming smaller for the smallest holes.

For each imaging method, the  $I_{Mean}$  will be determined first, as well as the SNR for each of the holes in the steel block. Where the SNR of the hole does not exceed 20 dB, the conclusion is that it is not possible to accurately determine the defect size because the noise and signal levels in the region near the defect are too similar. For images with holes exhibiting an SNR of at least 20 dB, a size will be estimated algorithmically. This is accomplished by establishing the defect's left, right, bottom, and top edges. This is detecting the left, bottom, right, and top pixels that satisfy an SNR that is at least 70% of the maximum SNR for that particular hole. After these pixels are determined, four "edges" are drawn around where the estimated defect location is, and their lengths are considered the length and height of the defect. The distance from the topmost edge to the surface of the block is considered the "depth" of the detected defect.

For the aluminum block, only the estimated size is known for the defects. Considering that the steel block provides a more rigorous test for accurately determining defect sizes, the aluminum block will only be analyzed by the SNR metric of the entire image.

### 3.6. Ultrasound signal processing

Before the ultrasound data are used in the imaging methodologies, the adjoint sources  $f_i^\dagger$  must first be evaluated for each source-receiver combination in the FMC for all time. Ideally,  $f_i^\dagger$  may be evaluated by implementing Eq. (26); further, this is an imperfect process in reality. An aspect of adjoint-source evaluation is that these data conditions operations consisting of filtering and windowing are usually applied [31]. In this application, a filtering scheme is implemented to remove the "direct arrivals" from the dataset. Because these direct arrivals near the phased-array aperture are significantly higher in magnitude than the reflected waves from defects, they will cause large artifacts within ARTM images near the phased-array aperture. This heavily incentivizes the use of filtering techniques to remove the direct arrivals before generating adjoint wavefields using a wave-equation simulator, e.g., SPECSEM2D. To ensure a valid comparison, the filtered data are also implemented in the TFM algorithm for consistency.

#### 3.6.1. Ultrasound signal processing: Numerical steel

Ultrasound signals are obtained from the defect-free model described in Table 4 while defect-containing signals are obtained using the externally generated mesh in Fig. 3. The data sizes between these two must be consistent for the adjoint source to be calculated. To allow this, the  $128 \times 128 \times 31250$  data cube described in Section 3.4 is subsampled to a  $dt$  of 2.5 ns from 0.48 ns resulting in a  $128 \times 128 \times 6000$  data volume. An example evaluation for source 12 in the 5 MHz phased-array is presented in Fig. 4 with the location is approximately shown in Fig. 5. A direct subtraction between Figs. 4(a) and 4(b) results in Fig. 4(c). However, due to the different mesh resolutions and  $dt$  size, direct arrival residuals are left. This can be removed through linear move-out (LMO) filtering because the direct arrivals propagate away from the source location as a linear band. The result after filtering is presented in Fig. 4(d). The LMO filtering process is repeated for each source in the phased array. A final processing step is a time-zero correction that advances the data forward by 0.2  $\mu$ s. The intent is to better align the source waveform with the distance calculation, allowing TFM to place more of the energy directly on the edge of the defect instead of delaying below it. To determine imaging accuracy, omitting this step would result in TFM producing an image with defects deeper than they are in the model.

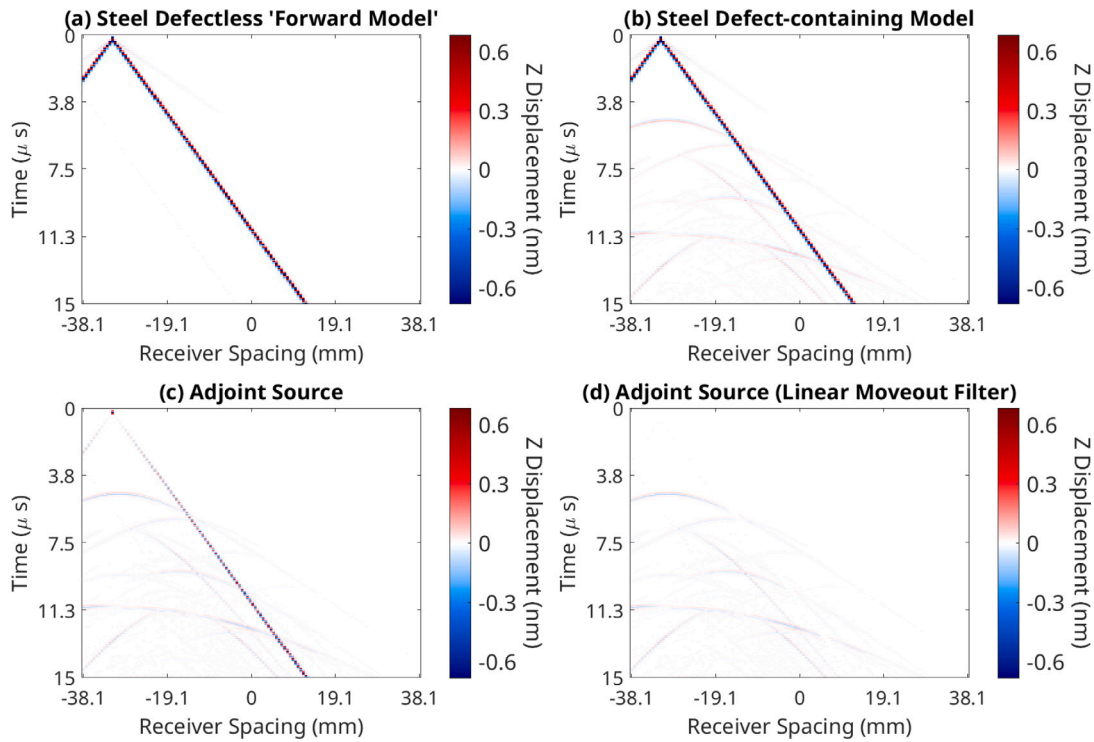


Fig. 4. Space-time signals for source 12 in numerical 5 MHz phased-array from (a) Defect-free and (b) Defect-containing models. (c) The adjoint source evaluated from (a) and (b). (d) The filtered adjoint source.



Fig. 5. 2D steel block diagram.

### 3.6.2. Ultrasound signal processing: Experimental steel

For cases with experimental data, the adjoint sources are formed using ultrasound data collected from the phased-arrays. In the numerical case, direct implementation of Eq. (26) without filtering would leave high-amplitude direct arrivals that would cause large image artifacts if not addressed. In addition, a linear move-out correction would not remove the direct waves presented in Fig. 6(a) for source 64 in the experimental dataset from the 5 MHz phased-array. The exact amplitude units for this data provided by AOS are unknown, so the data are normalized prior to filtering and implementation.

Processing steps for these data include applying time-gating and frequency-wavenumber filtering algorithms to reduce the presence of direct arrivals in the image. Fig. 6(b) presents the ultrasound data within the frequency-wavenumber domain (only showing positive frequencies). The regions underneath the black dashed lines are the coherent noise removed during the filtering process. Fig. 6(c) shows ultrasound data presented in Fig. 6(a) with a time-gating filter, and Fig. 6(d) shows the fully filtered signals after filtering of direct arrivals. The trade-off of this approach is that it removes some useful signals that may be within the similar frequency-wavenumber threshold, which can be observed by comparing Figs. 6(b) and 6(d). However, a large portion of the reflected signal from defects is preserved. A final change to the adjoint sources before implementation in ARTM is aligning it

with the STF implemented in the forward model. This involves shifting the dataset forward by  $0.03 \mu\text{s}$ . Similarly, the TFM will have its signal shifted forwards by  $0.52 \mu\text{s}$ . One final notable aspect is that the original dataset is  $30 \mu\text{s}$  long and is time-gated down to  $15 \mu\text{s}$ , which is shortly after the back wall reflection.

### 3.6.3. Ultrasound signal processing: “noisy” experimental steel

The third case study involves taking the previously filtered data in Section 3.6.2 and artificially reducing the signal SNR by increasing the root mean squared amplitude of the Gaussian noise added to the data. The SNR of a dataset is also evaluated using a modified version of Eq. (45)

$$\text{SNR} = 20 \log_{10} \left( \frac{|d_i|_{\max}}{|d_i|_{\text{Mean}}} \right). \quad (46)$$

where  $|d_i|_{\max}$  is the maximum signal in the data, which in this case is treated as the reflection from the largest hole, and  $|d_i|_{\text{Mean}}$  is the average noise. The goal is to generate a dataset with an  $\text{SNR} < 20 \text{ dB}$ . This is accomplished by adding random noise to the entire dataset using MATLAB’s “randn” function, omitting the region in the data where the initial zero filter is applied. Since the units of the signal are known, it is first normalized to the largest magnitude in that particular shot, which will be from the back wall. Notably, the maximum signal taken

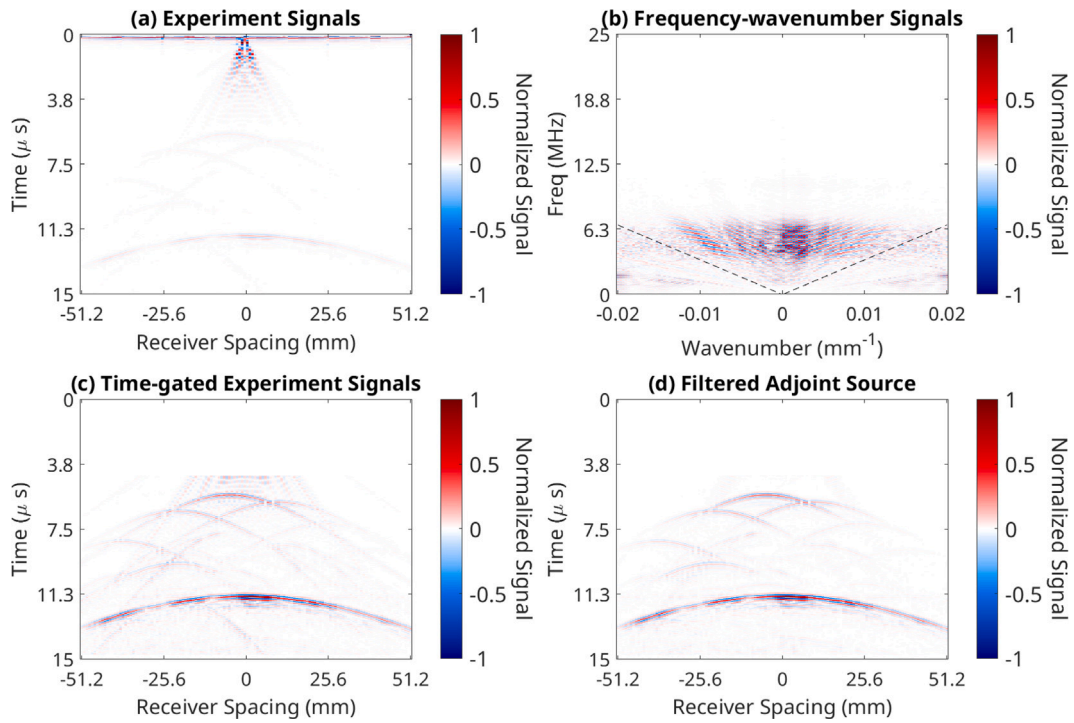


**Fig. 6.** Example filtering of 5 MHz ultrasound data for source 64. (a) Unfiltered time-domain signals and (b) frequency–wavenumber signals and filtering zone. (c) The time-domain signals with time gating. (d) The fully filtered adjoint source.

from this calculation is from the largest hole rather than the back wall, as that is a signal that is of interest. Fig. 7 shows different elements from the noise addition process. Fig. 7(a) presents the filtered and normalized ultrasound data from Section 3.6.2 for source 1. Fig. 7(b) shows the random noise added to Fig. 7(a) to produce Fig. 7(c), which is the noised data. Here, Fig. 7(b) is normalized by the magnitude of the backwall reflection in the same image. Within Fig. 7(c), the back wall reflection at  $\approx 11.3 \mu\text{s}$  while the first hole reflection at  $\approx 5.0 \mu\text{s}$  is barely visible. Fig. 7(d) presents the extracted 1-D signal from receiver 18 in Fig. 7(c). This process is repeated for every shot in the FMC, resulting in 128 different slices of “noisy” ultrasound data. The SNR of the dataset is approximate, as the true background noise is not discernible since perfectly removing the signal from the dataset would be impossible. An approximation of the background noise may be made by examining the average absolute noise and the maximum signal in the image (i.e.,  $d_{max}$  in Fig. 7(a)), not counting the back wall reflection. This reflected signal is from the largest hole, which is  $\approx 0.3$  the magnitude of the backwall signal. The average unit-normalized absolute noise added to the signal lies between  $[0.086–0.088]$ ; if this average is considered  $d_{Mean}$ , then the signal SNR implemented in this study should be approximately 10.7 dB as evaluated in Eq. (46).

### 3.6.4. Ultrasound signal processing: Experimental aluminum

For the aluminum domain, a different forward model is implemented to generate synthetic observed signals  $d_i^M(x_r, t)$  and forward wavefields  $s_i(x, t)$ . The specific model is outlined in Table 4. The experimental data is from the 3 MHz phased array. Again, the true data units provided by AOS are unknown, so they are first normalized. Similarly to the experimental data from the steel block, filtering must be implemented first for a useful adjoint source  $f_i^\dagger$  to be evaluated. The same approach implemented in Section 3.6.2 is applied to the ultrasound data from the 3 MHz phased array. Fig. 8(a) presents the unfiltered signals from source 64. Fig. 8(b) is the corresponding ultrasound data in the frequency–wavenumber domain with only positive frequencies being shown. Fig. 8(c) presents the data with a time filter

for the initial data sections, and Fig. 8(d) presents the filtered adjoint sources implemented in the ARTM process. Like the prior case, the signals are time-shifted forward by  $0.03 \mu\text{s}$  for the ARTM algorithm and by  $0.52 \mu\text{s}$  for the TFM analysis.

## 3.7. ARTM & TFM implementation

### 3.7.1. ARTM implementation

Implementation of ARTM consists of three different parts: (1) generation of forward wavefields  $s_i(x, t)$ , (2) generation of adjoint wavefields  $r_i^\dagger(x, t)$ , (3) cross-correlation at each time step, and (4) summation of images from each source location. 2D wavefield simulations are completed in SPEC-FEM2D. The simulation is oriented normal to the phased-array surface into the domain of the material, with depth being represented by  $z$  and along the phased-array aperture being represented by  $x$ . For a particular source transducer location in the phased arrays described in Table 3, a point force is modeled as a Ricker wavelet with a corresponding central frequency, i.e., 5 MHz for steel and 3 MHz for aluminum. This force source is inserted into a SPEC-FEM2D simulation while acting purely in the  $z$ -direction. The mesh and material properties correspond to the defect-free internally meshed version of the domain described in Table 4. For each time increment described in Table 4, a forward wavefield  $s_i(x, t)$  is generated. Simultaneously, the SPEC-FEM2D simulates an adjoint wavefield  $r_i^\dagger(x, T-t)$ . At all transducer locations in the phased-arrays described in Table 3 the adjoint-sources evaluated in Section 3.6 are injected at each corresponding receiver location, acting as several vertical point forces acting in the  $z$ -direction. Notably, the adjoint sources are time-reversed before being injected into the domain. The mesh and material properties for the adjoint wavefield simulation are identical to those of the forward model. Because of the parallel simulations, the cross-correlation conditions described in Eqs. (29), (37) and (39) may be evaluated at each time step. This is repeated for all  $N_T$  time steps described in Table 4, with the stacked sum representing the imaging kernels (i.e.,  $K_{V_p}$ ,  $K_{V_s}$ ,  $K_\rho$ , and  $K_\rho'$ ), pertaining to that particular source location. This process is repeated

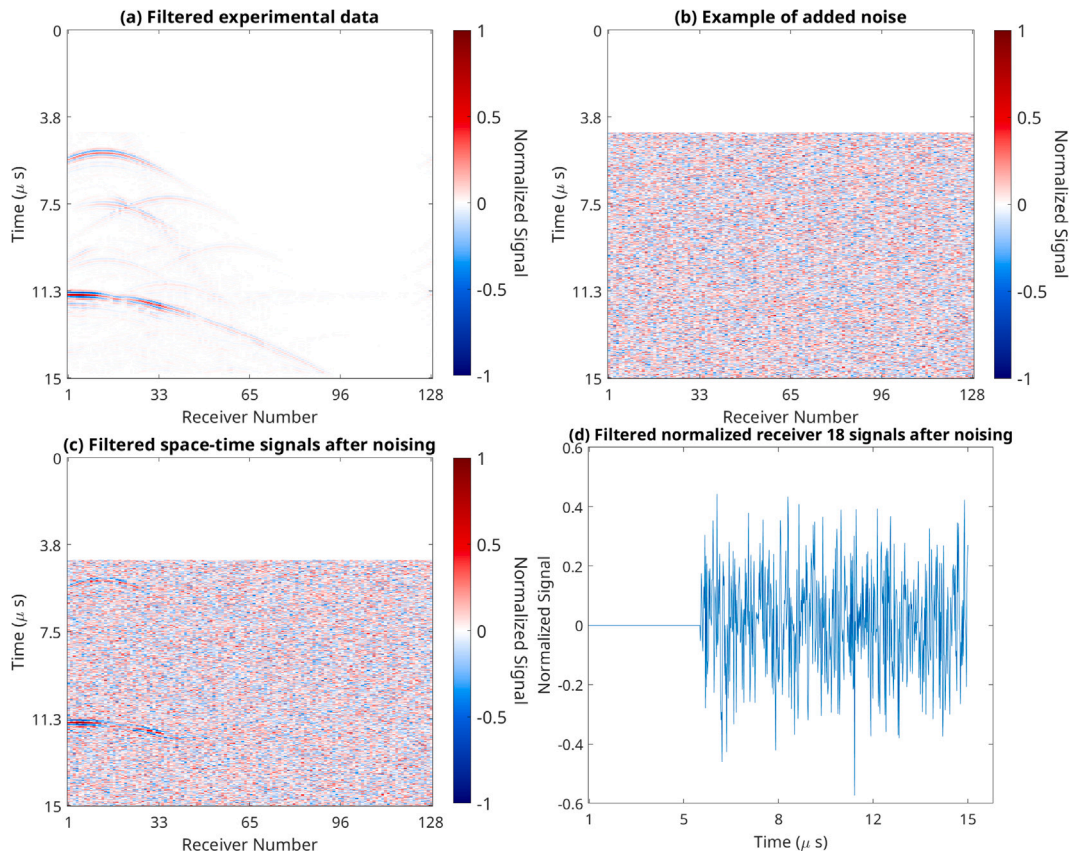


Fig. 7. Noise addition process for “noisy” steel dataset: (a) filtered normalized ultrasound data from source 1, (b) example noise added to each source, (c) example “noisy” space–time signals for source 1, and (d) example “noisy” 1-D signal for source 1 receiver 18 combination.

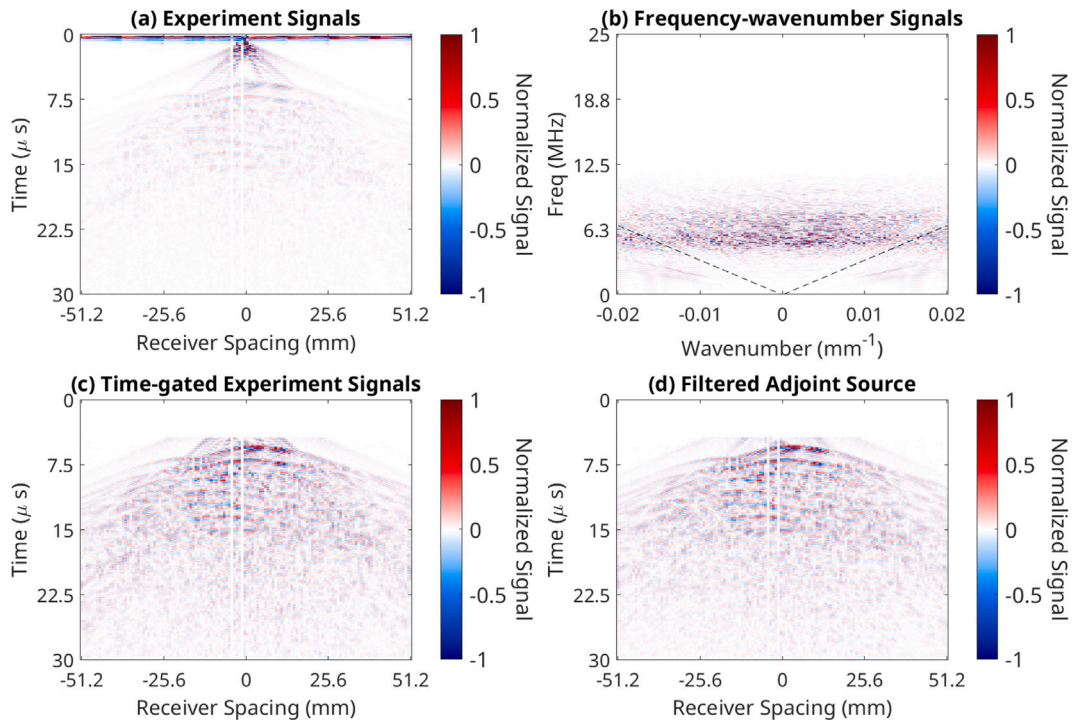


Fig. 8. Example filtering of 5 MHz ultrasound data for source 64. (a) Unfiltered time-space and (b) frequency–wavenumber signals and filtering zone. (c) The time-domain signals with time gating. (d) The fully filtered adjoint source.

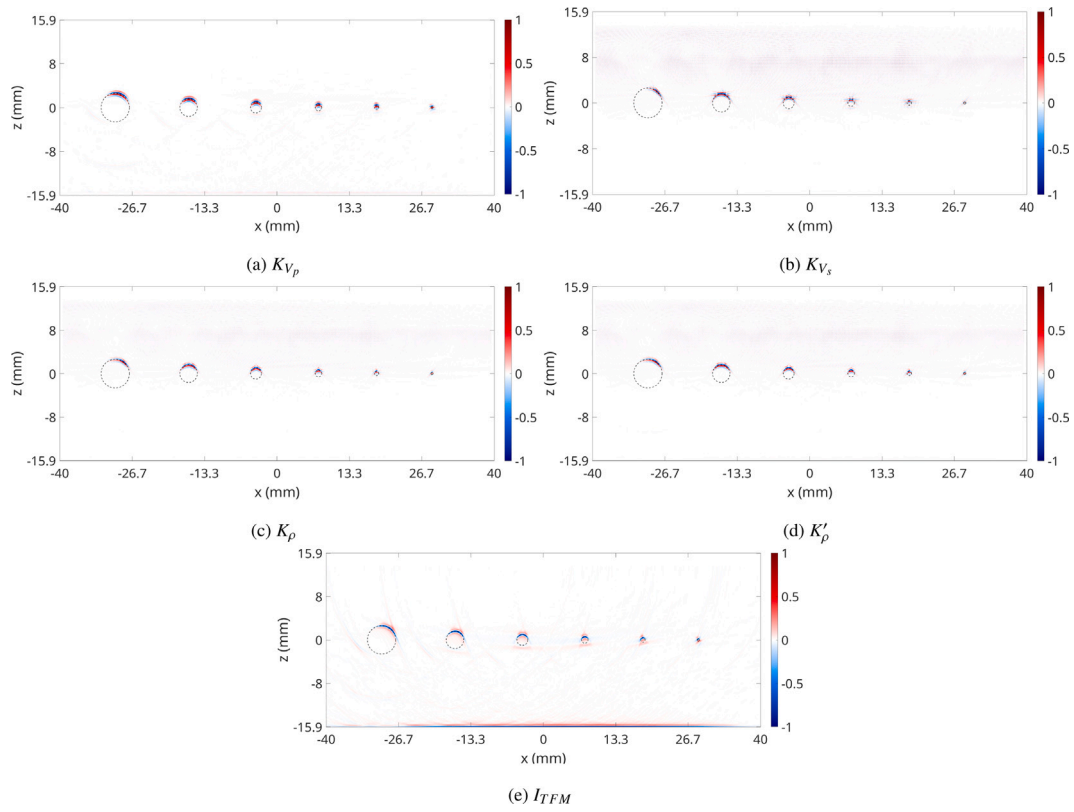


Fig. 9. ARTM results for numerical steel data with sensitivity kernels: (a)  $K_{V_p}$ , (b)  $K_{V_s}$ , (c)  $K_{\rho}$ , (d)  $K'_{\rho}$ , and (e)  $I_{TFM}$ .

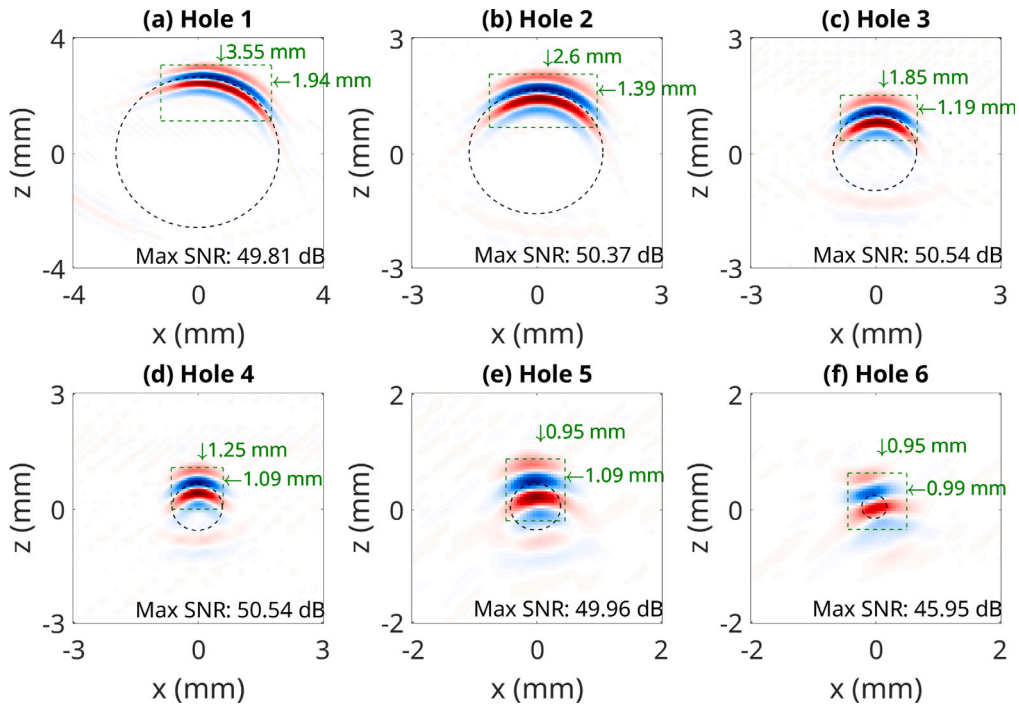


Fig. 10. Zoomed in numerical steel images for each hole within  $K_{V_p}$ .

for all transducers in the phased-arrays and all sub-images are directly added for a particular kernel, which results in the final defect images.

For the numerical steel block case, the “Steel” simulation described in Table 4 is implemented for both forward and adjoint wavefields. For adjoint sources  $f_i^{\dagger}$ , the processed ultrasound data represented in

Fig. 4 are injected into the domain for adjoint-wavefield simulation. This process is repeated for both the experimental steel studies and the “noisy” experimental steel study. The only difference in methodology for these two studies compared to the numerical case is the particular adjoint-source implemented. For the experimental steel case, the data

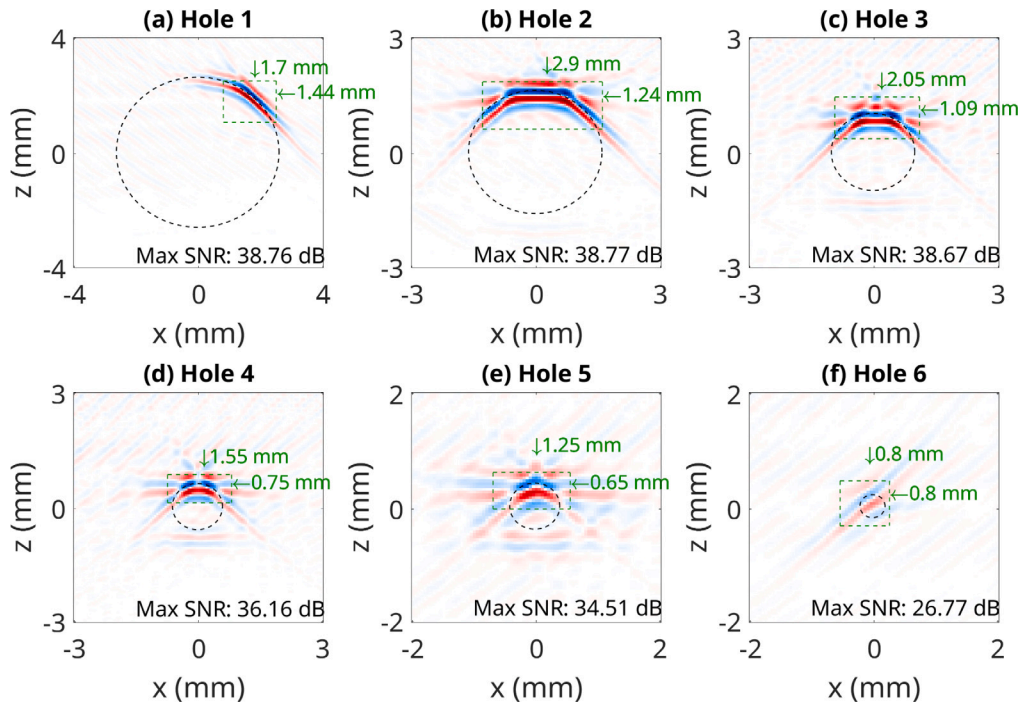


Fig. 11. Zoomed in numerical steel images for each hole within  $K_{V_z}$ .

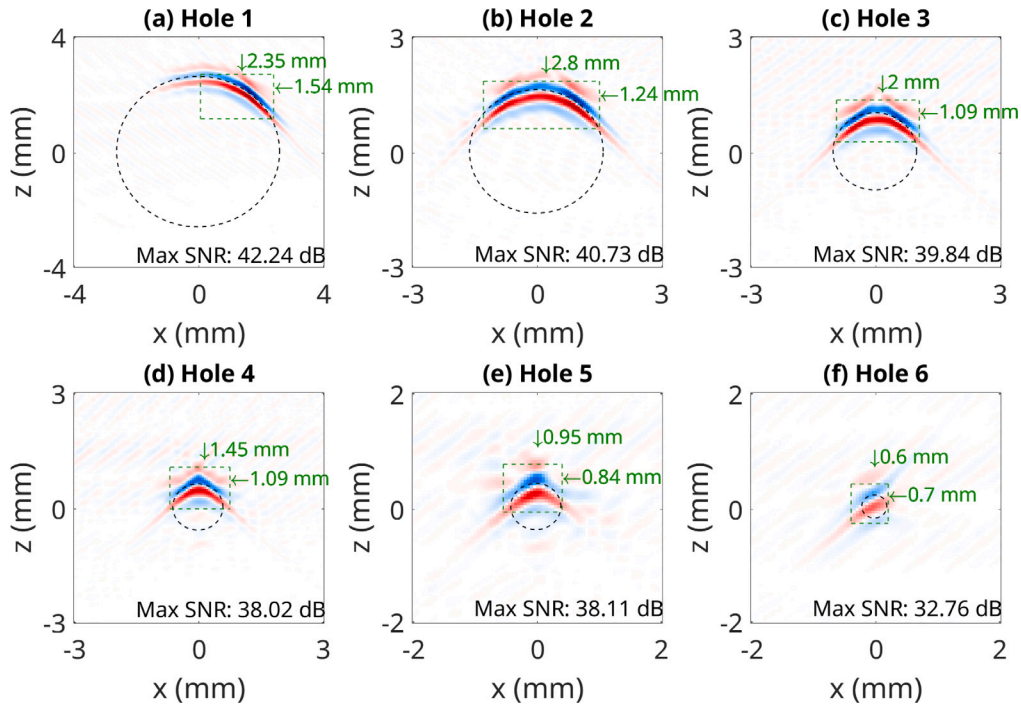


Fig. 12. Zoomed in numerical steel images for each hole within  $K_{\rho}$ .

described in Fig. 6 are used, while the “noisy” steel case involves data from Fig. 7. With these three studies, three sets of images from the  $K_{V_p}$ ,  $K_{V_z}$ ,  $K_{\rho}$ , and  $K_{\rho}'$  kernels are generated and presented in each section.

For the aluminum block case, the “Aluminum” simulation described in Table 4 is implemented for both forward and adjoint-wavefields in a similar manner. The differences between this and the prior scenario are: (1) the central transducer frequency is 3 MHz instead of 5 MHz, (2) the material properties and geometry of the simulation represents the

aluminum block instead of the steel one, (3) the phased-array aperture and transducer locations, and (4) the simulation time and time step size corresponds to the “Aluminum” simulation described in Table 4.

A final aspect is that transducers transmit waves into the specimen via coupling gel, meaning the waves penetrate the gel before entering the domain or returning to the transducer surface. This interaction was not modeled during numerical source excitation; instead, the sources and receivers are placed at the top of the domain as if they were

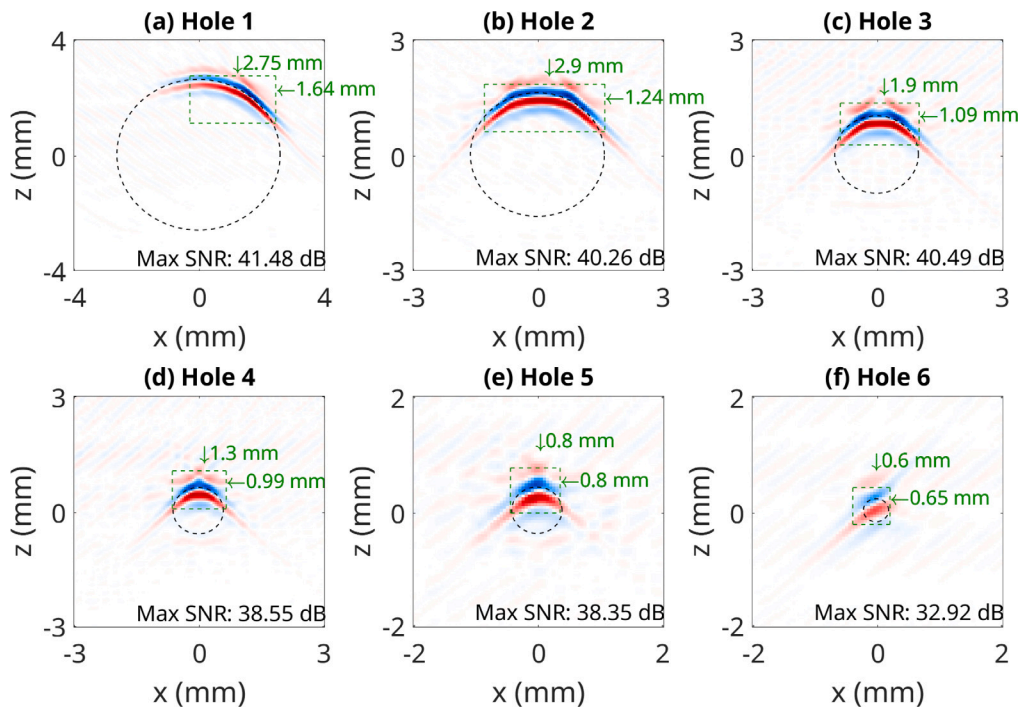


Fig. 13. Zoomed in numerical steel images for each hole within  $K'_p$ .

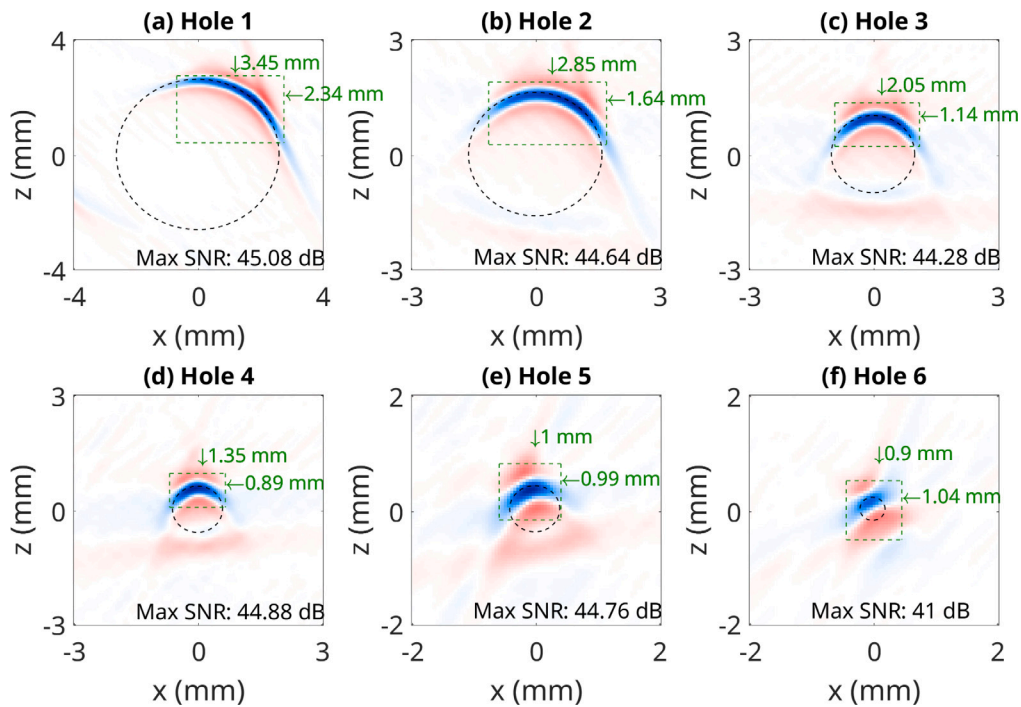


Fig. 14. Zoomed in numerical steel images for each hole within  $I_{TFM}$ .

on the boundary of the specimen being scanned. Thus, this approximation makes two assumptions: (1) the surficial interactions will not significantly limit wave propagation into or out of the domain, and (2) the elapsed time taken for waves to travel into and out of the domain is significantly smaller than the duration spent to and from the internal defects. If these assumptions are met, the defect location and

size detection should not be adversely affected, as demonstrated in the results.

### 3.7.2. TFM implementation

TFM is implemented for each case as well to serve as a baseline. The methodology for TFM follows the process outlined in Section 2.4,

**Table 5**  
Location and sizing comparisons for numerical steel images.

| Hole:     | 1     |        |       | 2     |        |       | 3     |        |       |
|-----------|-------|--------|-------|-------|--------|-------|-------|--------|-------|
| Quantity: | Width | Height | Depth | Width | Height | Depth | Width | Height | Depth |
| $K_{V_p}$ | 3.55  | 1.94   | 12.89 | 2.60  | 1.39   | 13.89 | 1.85  | 1.19   | 14.44 |
| $K_{V_s}$ | 1.70  | 1.44   | 13.44 | 2.90  | 1.24   | 14.09 | 2.05  | 1.09   | 14.49 |
| $K_p$     | 2.35  | 1.54   | 13.24 | 2.80  | 1.24   | 14.09 | 2.00  | 1.09   | 14.59 |
| $K'_p$    | 2.75  | 1.64   | 13.19 | 2.90  | 1.24   | 14.09 | 1.90  | 1.09   | 14.59 |
| $I_{TFM}$ | 3.45  | 2.34   | 13.19 | 2.85  | 1.64   | 14.04 | 2.05  | 1.14   | 14.59 |
| Measured  | 5.2   | 5.2    | 13.3  | 3.2   | 3.2    | 14.3  | 2.0   | 2.0    | 14.9  |
| Hole:     | 4     |        |       | 5     |        |       | 6     |        |       |
| Quantity: | Width | Height | Depth | Width | Height | Depth | Width | Height | Depth |
| $K_{V_p}$ | 1.25  | 1.09   | 14.89 | 0.95  | 1.09   | 15.09 | 0.95  | 0.99   | 15.34 |
| $K_{V_s}$ | 1.55  | 0.75   | 15.09 | 1.25  | 0.65   | 15.34 | 0.80  | 0.80   | 15.49 |
| $K_p$     | 1.45  | 1.09   | 14.89 | 0.95  | 0.84   | 15.19 | 0.60  | 0.70   | 15.54 |
| $K'_p$    | 1.30  | 0.99   | 14.89 | 0.80  | 0.80   | 15.19 | 0.60  | 0.65   | 15.54 |
| $I_{TFM}$ | 1.35  | 0.89   | 14.99 | 1.00  | 0.99   | 15.14 | 0.90  | 1.04   | 15.44 |
| Measured  | 1.2   | 1.2    | 15.3  | 0.8   | 0.8    | 15.5  | 0.4   | 0.4    | 15.7  |

where the time-of-flight (TOF) for each source-receiver combination is evaluated for a discretized domain  $\mathbf{x}$ . This TOF considers solely the longitudinal wave speed of the material presented in Table 1. The discretized domain  $\mathbf{x}$  has the same resolution as the corresponding ARTM images to allow a direct comparison. The TFM images corresponding to the ARTM studies are presented in the corresponding sections alongside the kernels.

#### 4. Results

This section presents the numerical and experimental ARTM results obtained from the data acquisition and imaging kernels described above for four parameters: longitudinal wave speed, shear wave speed, density, and impedance. These results are compared with those from the TFM imaging method, which was implemented as a baseline for comparison to the ARTM methods.

##### 4.1. Steel block defect images

Figs. 9, 15 and 21 contain the ARTM-generated images from ultrasound data from the steel block. Images were generated from three ultrasound data sets: (1) numerically generated based on the transducer and steel block geometry, (2) acquired from the steel block using a phased-array transducer, and (3) the laboratory data from (2) after contaminating the data to artificially reduce the SNR. A comparative analysis of the ARTM kernels and TFM results is conducted based on three criteria: (1) accuracy in sizing, (2) accuracy in depth positioning, and (3) the maximum SNR achieved. Additionally, the required time to generate images for each specimen is discussed; this is not repeated for each steel block case, as the speed is about the same. Sizing and positioning of defects are of interest for NDE research purposes, and in some studies SNR is employed as an atypical metric [43]. To determine whether an image provides accurate hole location estimates, the true position from physical measurements is superimposed on the ARTM-generated images. This allows direct comparison of the estimated and real locations based on measurements, allowing visual inspection of image accuracy. In addition, the sizing is estimated using the methodology described in Section 3.5 and tabulated for each hole to determine which imaging method most accurately determined defect characteristics.

##### 4.1.1. Steel images from numerically generated data

Inspection of the results shown in Fig. 9 suggests that each imaging condition performs similarly on numerical data. The numerical results represent an idealized modeling scenario because the user-specified STF, the true source and receiver positions, and the boundary locations are all known in advance. TFM is also implemented in this study within Fig. 9(e). If only the negative image amplitudes were considered, the

TFM method would have superior resolution compared to the kernels; however, the positive image amplitudes would lead to less accurate contour determinations. A limitation of all imaging methods is the coverage of the array. The holes with better coverage consistently have a better depiction of what their width should be, whereas the defects with poor coverage, such as the larger holes on the left, are significantly underpredicted across all methods. This limitation extends to the later results when experimental data is implemented.

To better determine the sizing of the defects within each image, a closer depiction of each hole from each image is provided in Figs. 10 to 14. Table 2 lists the holes labeled 1–6 as well as the SNR of the individual hole’s maximum amplitude. Failing to achieve a SNR of  $> 20$  dB will impede algorithmically determining the hole counter. Table 5 presents a summary of the accuracy in sizing and depth of the defect, where “Measured” is the size of the hole based upon the experimental measurements with calipers. For the numerical test, this can be treated as a true value. The results are indicative that the shear wave speed kernel (Fig. 11) exhibits the best resolution, likely due to the wavelength of the shear wave being approximately half the longitudinal wave length. At the same time, though, it has a poor representation of the first and last holes, likely because of the comparably limited coverage. This results in the sizing estimates being more accurate for defects immediately under the transducer and poorer for those further away. The longitudinal wave speed kernel (Fig. 10) has the poorest resolution in terms of the defect contour; however, it does yield accurate sizing estimates of a majority of defects with good coverage except for the smallest hole. The three kernels  $K_{V_p}$ ,  $K_p$ , and  $K'_p$  (Figs. 10, 12 and 13) extend the image of the largest hole the farthest to the left (hole 1), while  $K_{V_s}$  and  $I_{TFM}$  (Figs. 11 and 14) stop showing significant amplitude closer to the center of the largest hole. Imaging the smallest hole is performed well via  $K_p$ , and  $K'_p$  (Figs. 12 to 13). The imaging method that performs most optimally is highlighted and has green text. This is repeated for all the holes in each image. The most accurate method to characterize hole depth is between  $K_{V_s}$ ,  $K_p$ , and  $K'_p$  (Figs. 11 to 13) for different holes while  $I_{TFM}$  performs similarly to  $K_{V_p}$ .  $K_{V_p}$  performs the worst when determining the accurate defect depth, even in this case where the background wave speed and STF are predefined.

The maximum SNR of the entire image is used as a metric of comparison. This requires quantifying the mean amplitude assigned away from defected regions. This metric is evaluated for  $K_{V_p}$ ,  $K_{V_s}$ ,  $K_p$ ,  $K'_p$ , and  $I_{TFM}$  from Fig. 9. The back wall is not considered when evaluating the average amplitude of the background noise. Table 6 presents the corresponding SNRs, which show that the ARTM-based imaging methods have a higher SNR and fewer overall artifacts compared to TFM. Among the kernels,  $K_{V_p}$  has the lowest average noise.

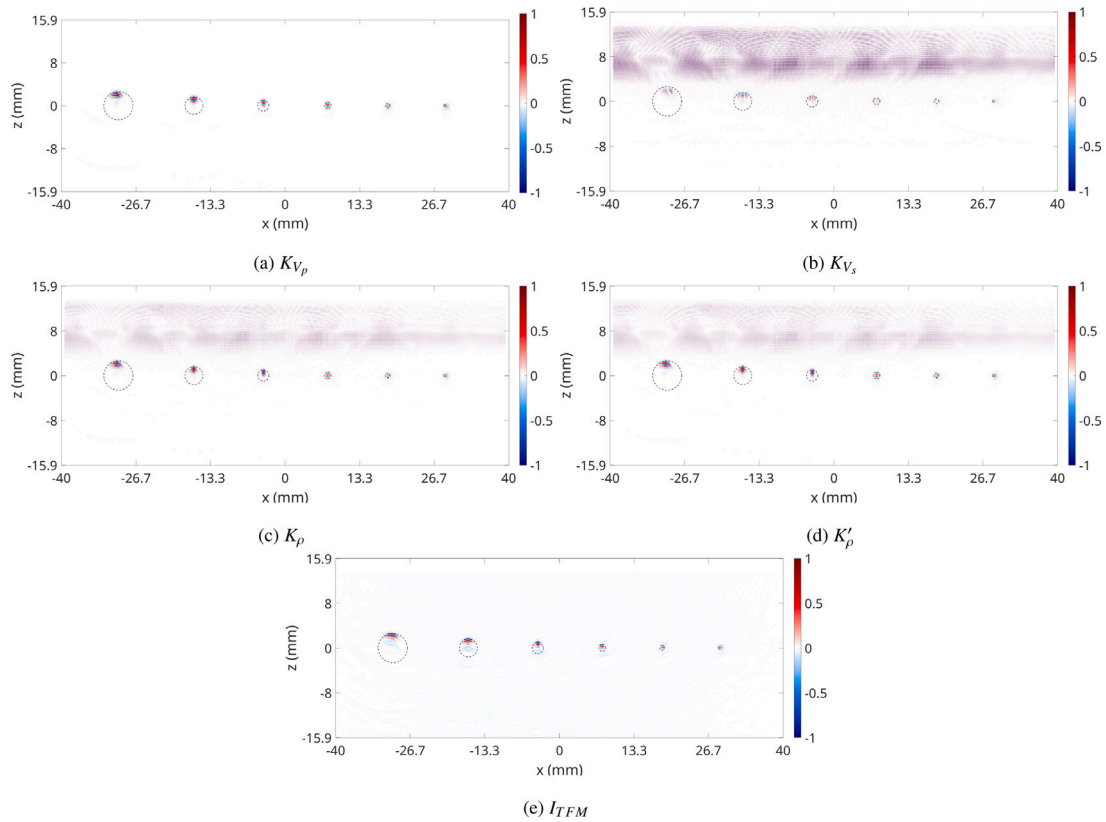


Fig. 15. ARTM results for experimental steel data with sensitivity kernels: (a)  $K_{V_p}$ , (b)  $K_{V_s}$ , (c)  $K_\rho$ , and (d)  $K'_\rho$ . (e) TFM Image.

Table 6

Maximum SNR of numerical steel block images.

| Imaging Method | SNR (dB) |
|----------------|----------|
| $K_\rho$       | 41.65    |
| $K_{V_p}$      | 52.36    |
| $K_{V_s}$      | 40.58    |
| $K'_\rho$      | 41.64    |
| $I_{TFM}$      | 35.65    |

From the numerical studies, it is concluded that the majority of ARTM kernels perform similarly in sizing tasks.  $K_{V_p}$  performed well to size the largest hole, which has the least coverage. It was less effective at sizing holes with better coverage toward the center of the transducer, with  $K_{V_s}$  and  $K_{V_p}$  being better for the second and third holes, respectively. For small holes,  $K'_\rho$  more consistently yielded the best results. Compared to TFM, the kernel methods have less noise in their final image while providing a superior resolution depending on the size of the defect and kernel implemented.

The time required to generate images is an important factor for NDE implementation. Both methods can be massively parallelized or GPU-enabled, so in order to isolate the impact of the method's computational complexity, the time taken for each algorithm to generate an image from a single source is provided. This time is derived from the average time for a source-wise image to be generated based on 10 different runs using a single core on an Intel(R) Xeon(R) Silver 4214 CPU @ 2.20 GHz. The TFM algorithm only required about 5.50 s per source, while the ARTM algorithm required about 885 s per source. This reinforces the understanding that a TFM algorithm will be significantly faster than the ARTM algorithm, especially without implementing any heterogeneous model. However, the performance of both algorithms will vary depending on the implementation, especially what finite-element solver is used to generate the wavefields.

#### 4.1.2. Steel images with experimental laboratory data

Fig. 15 presents the ARTM results generated from the steel block experimental signals. To facilitate benchmarking, each image has the actual hole locations from Table 2 superimposed upon the images as black circles. A surface-level analysis reveals that the longitudinal wave speed kernel (Fig. 15(a)) outperforms the other kernels. Numerous artifacts are present within Fig. 15(b)–(d), which could be considered false positives for boundaries of different materials. However, these images still provide a similar image to that of Fig. 15(a) at near-hole locations. Notably, Fig. 15(a) does not contain significant artifacts, which will be reflected in the total image SNR estimate. In contrast to [24], the imaging condition with the fewest artifacts is derived from  $K_{V_p}$  instead of  $K'_\rho$ , which was demonstrated to have artifact-canceling attributes in that study. The findings here are less conclusive as to why this is the case. A notable difference between the implementation in this work and that of [24] is the simplicity of the model parameters, which only contain a single wave speed set and density, in contrast to [24] which implements it in seismological models with various different regions with different densities and wave speeds. The TFM performance shown in Fig. 15(e) is as expected, as it reliably detects the hole contours and, on brief inspection, provides an image of similar quality to Fig. 15(a). For these experimental datasets, while the background noise and imaging method influence the resulting image, the accuracy in imaging depth and sizing is directly dependent on a correct prediction of material properties, e.g., background wave speeds and density (see Figs. 17–19).

To quantify the accuracy of different kernels, their accuracy in characterizing the hole width, height, and depth is evaluated. To facilitate this, the areas in the images presented in Fig. 15 are extracted and presented in Figs. 16–20. The original hole position is again superimposed on the image as a black circle. A green box outlines the estimated hole dimensions from the ARTM or TFM-generated image. Notably, each method underestimates the size and overestimates the width of the

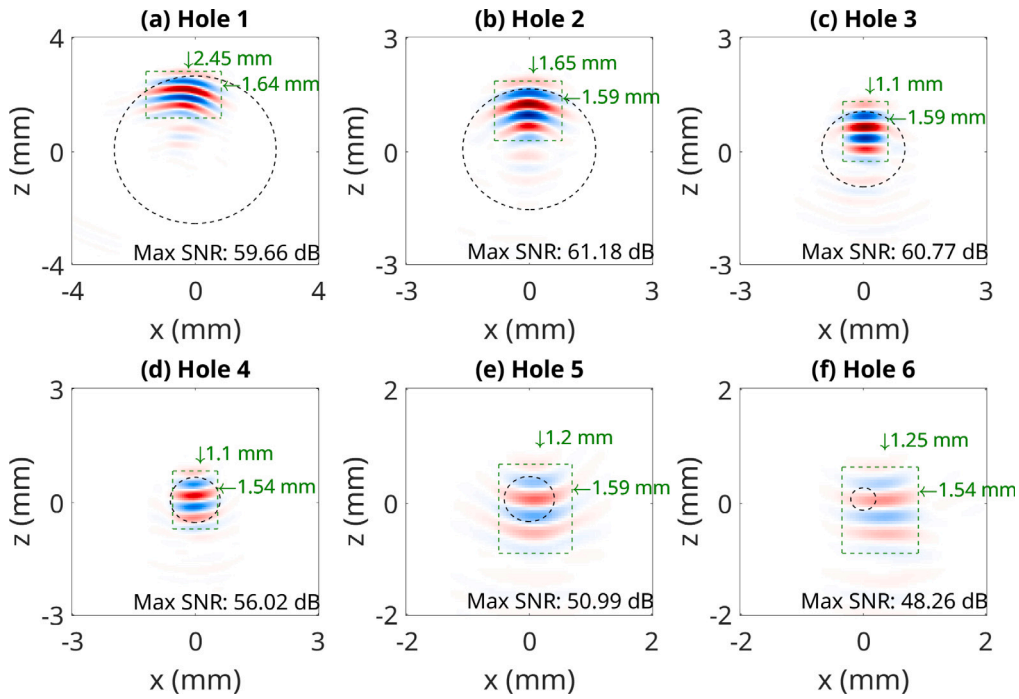


Fig. 16. Zoomed in experimental steel images for each hole within  $K_{V_p}$ .

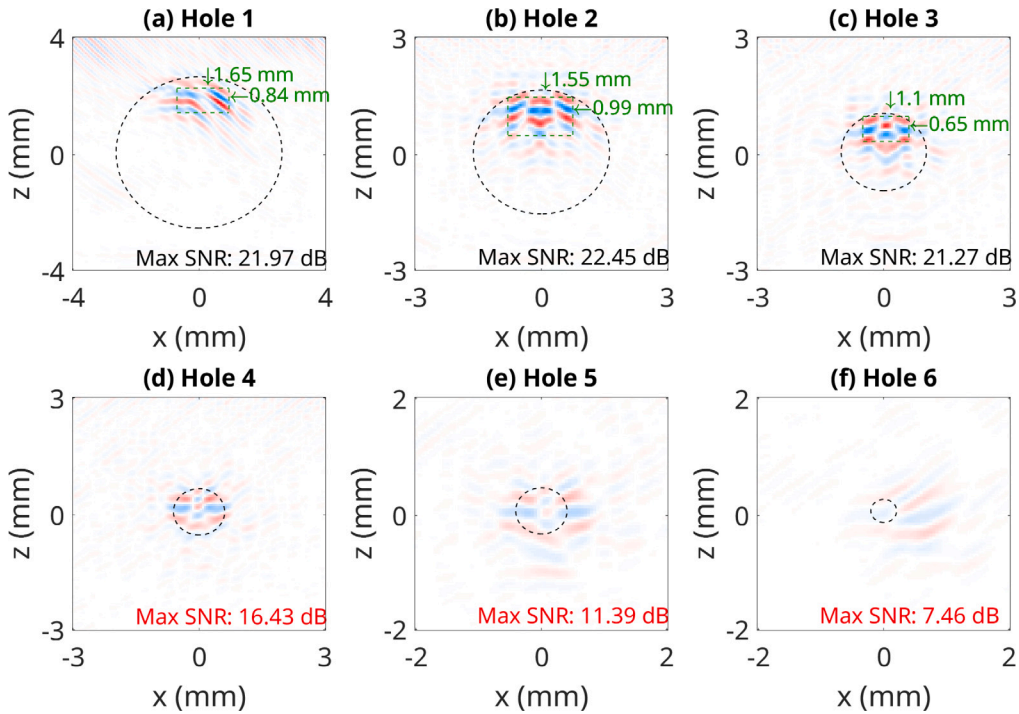


Fig. 17. Zoomed in experimental steel images for each hole within  $K_{V_s}$ .

largest hole while overestimating the size of the smallest. This is likely due to the illumination of the holes on the edge being significantly less than those in the center. The sizing and location information is also presented in Table 7.  $K_{V_p}$  provides accurate size estimation for the larger holes, although it is the least accurate at characterizing smaller holes. For smaller holes, it is apparent that  $K_p$  and  $I_{TFM}$  perform best. Imaging depth accurately was most common in  $K_p$  and was more accurate than  $I_{TFM}$  in all except one.

A final metric to benchmark the experimental ultrasound images is quantifying the mean noise in the image via the SNR. This is evaluated for all images in Fig. 15 and displayed in Table 8. The SNR of the  $K_{V_s}$ ,  $K_p$ , and  $K'_p$  kernels are lower than  $K_{V_p}$  and  $I_{TFM}$ . This is reinforced by the presence of large artifacts at the top of the images presented in Fig. 15(b)–(d) that are absent in Fig. 15(a) and Fig. 15(e).

Between the numerical (Fig. 9) and experimental (Fig. 15) results, the kernels perform similarly, with the image quality for  $K_{V_s}$  degrading more than expected. While the ARTM results were similar in both cases,

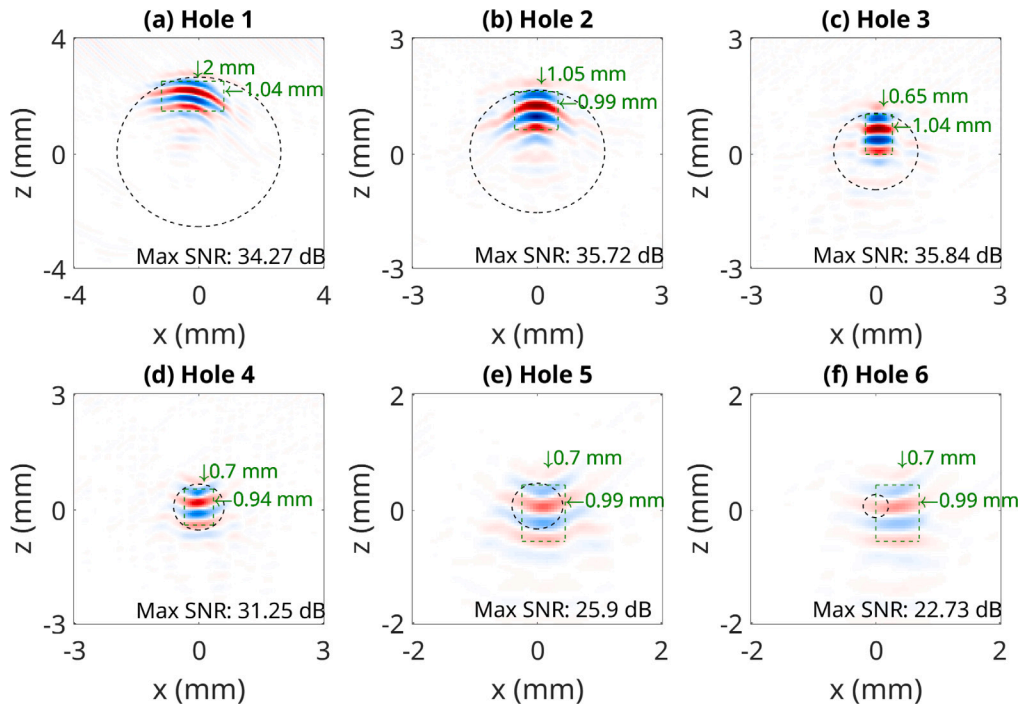


Fig. 18. Zoomed in experimental steel images for each hole within  $K_p$ .

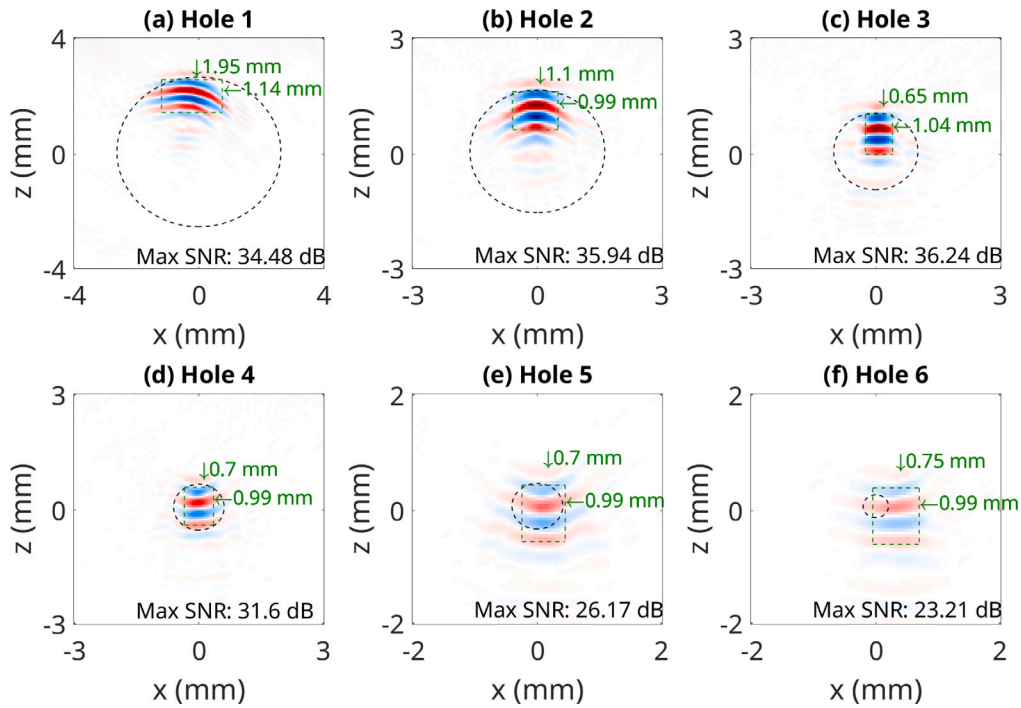


Fig. 19. Zoomed in experimental steel images for each hole within  $K'_p$ .

a significant difference was the ultrasound data source used to generate the adjoint sources. Ultrasound data are generated using an acoustic waveform that is not fully characterized as established in Section 3.7.1. In the numerical case, the acoustic waveforms ideally match those used to forward model data and wavefields. It is notable that there is a significant increase in the amount of noise between Tables 6 and 8. A consistency between the two is that the  $K_{V_p}$  kernel contains a

comparably lower amount of average background noise, indicating it has fewer artifacts.

#### 4.1.3. Steel images with “noisy” experimental laboratory data

A final study using the steel block model is the implementation of the imaging techniques using a dataset that has an artificially lowered SNR. Fig. 21 presents the imaging results. The addition of noise to the

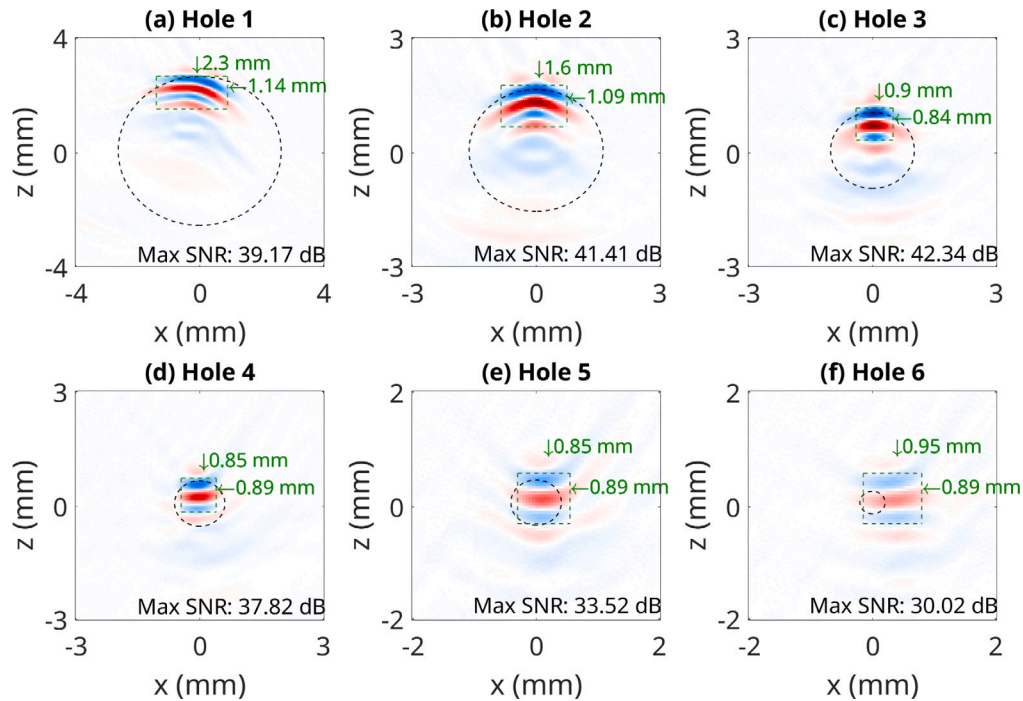


Fig. 20. Zoomed in experimental steel images for each hole within  $I_{TFM}$ .

Table 7  
Location and sizing comparisons for experimental steel images.

| Hole:     | 1     |        |       | 2     |        |       | 3     |        |       |
|-----------|-------|--------|-------|-------|--------|-------|-------|--------|-------|
| Quantity: | Width | Height | Depth | Width | Height | Depth | Width | Height | Depth |
| $K_{V_p}$ | 2.45  | 1.64   | 13.14 | 1.65  | 1.59   | 14.09 | 1.10  | 1.59   | 14.64 |
| $K_{V_s}$ | 1.65  | 0.84   | 13.69 | 1.55  | 0.99   | 14.49 | 1.10  | 0.65   | 14.99 |
| $K_p$     | 2.00  | 1.04   | 13.44 | 1.05  | 0.99   | 14.34 | 0.65  | 1.04   | 14.94 |
| $K'_p$    | 1.95  | 1.14   | 13.39 | 1.10  | 0.99   | 14.34 | 0.65  | 1.04   | 14.94 |
| $I_{TFM}$ | 2.30  | 1.14   | 13.29 | 1.60  | 1.09   | 14.19 | 0.90  | 0.84   | 14.79 |
| Measured  | 5.2   | 5.2    | 13.3  | 3.2   | 3.2    | 14.3  | 2.0   | 2.0    | 14.9  |
| Hole:     | 4     |        |       | 5     |        |       | 6     |        |       |
| Quantity: | Width | Height | Depth | Width | Height | Depth | Width | Height | Depth |
| $K_{V_p}$ | 1.10  | 1.54   | 15.14 | 1.20  | 1.59   | 15.29 | 1.25  | 1.54   | 15.34 |
| $K_{V_s}$ | ND    | ND     | ND    | ND    | ND     | ND    | ND    | ND     | ND    |
| $K_p$     | 0.70  | 0.94   | 15.43 | 0.70  | 0.99   | 15.54 | 0.70  | 0.99   | 15.54 |
| $K'_p$    | 0.70  | 0.99   | 15.38 | 0.70  | 0.99   | 15.54 | 0.75  | 0.99   | 15.59 |
| $I_{TFM}$ | 0.85  | 0.89   | 15.24 | 0.85  | 0.89   | 15.39 | 0.95  | 0.89   | 15.39 |
| Measured  | 1.2   | 1.2    | 15.3  | 0.8   | 0.8    | 15.5  | 0.4   | 0.4    | 15.7  |

Table 8  
Maximum SNR of experimental steel block images.

| Imaging Method | SNR (dB) |
|----------------|----------|
| $K_p$          | 37.23    |
| $K_{V_p}$      | 61.61    |
| $K_{V_s}$      | 24.70    |
| $K'_p$         | 37.60    |
| $I_{TFM}$      | 43.75    |

images has made the artifacts worse in cases Fig. 21(b)–(d), suggesting that the noise in the ultrasound data is the likely cause of the artifacts from the prior experimental data in Fig. 15(b)–(d).  $K_{V_s}$  (Fig. 21(b)) has artifacts that prevent the last holes from being seen at all, and all holes have an SNR of < 20 dB. An apparent downside of  $K_{V_s}$  as an imaging condition is that when noise is introduced, its performance drastically reduces in comparison to the other kernels. In Fig. 9(b), it was one of

the best imaging conditions for determining an accurate contour of the holes; however, in Fig. 15(b), it becomes significantly less preferable. Finally, in Fig. 21(b), the image fails to represent the holes entirely. Figs. 21(a) and 21(e) contain the least obscuring artifacts. However, the TFM image (Fig. 21(e)) has significantly more background artifacts than previously in Fig. 15(e). Figs. 22–26 provide zoomed-in images for determining hole size and depth. Table 9 presents a measurement comparison.

For defect sizing estimates, the addition of noise has degraded each image to the point that only the smallest hole image has an SNR greater than 20 dB for  $K_{V_p}$ . In the rest of the cases, all images except  $K_{V_s}$  are able to have an estimated hole size extrapolated. The preferred methods in this case are  $I_{TFM}$  and  $K_{V_p}$  overall. For the second-smallest hole,  $K_p$  performs best, repeating the trend from prior studies.

The final comparison metric for the images presented in Fig. 21 is the relative average background noise. The results are presented in Table 10. The results are consistent with Table 8, with  $K_{V_s}$ ,  $K_p$ ,

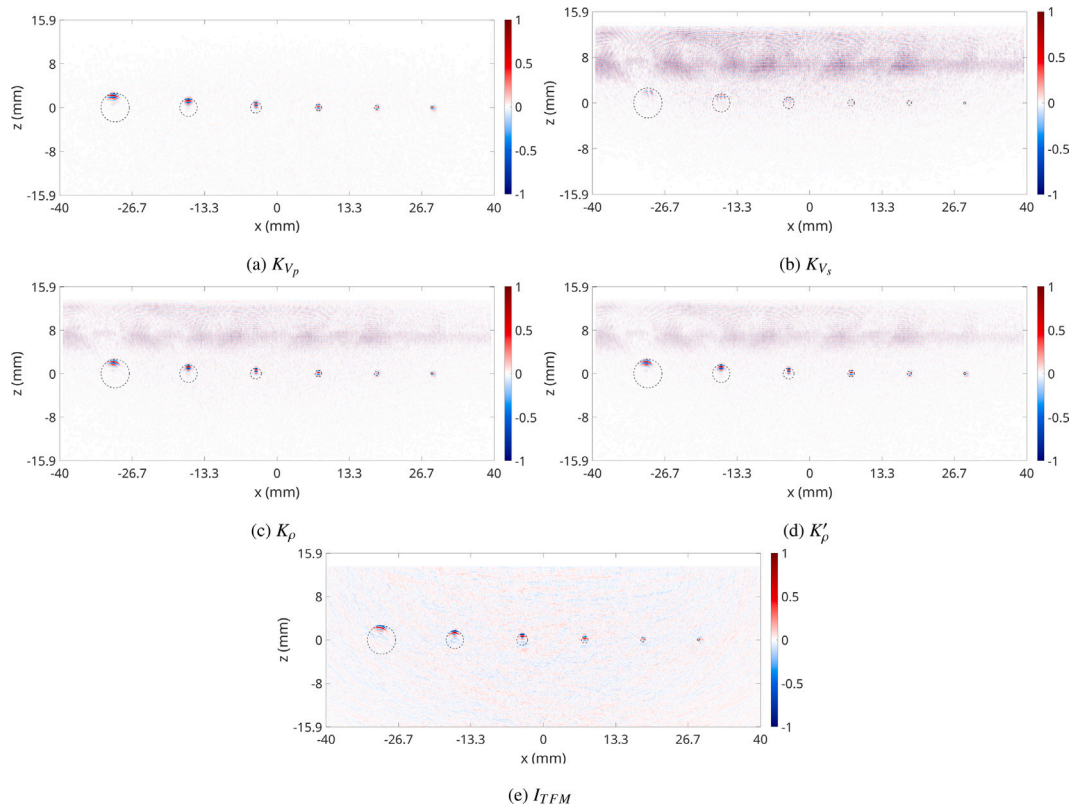


Fig. 21. ARTM results for “noisy” experimental steel data with sensitivity kernels: (a)  $K_{V_p}$ , (b)  $K_{V_s}$ , (c)  $K_p$ , and (d)  $K'_p$ . (e) TFM image.

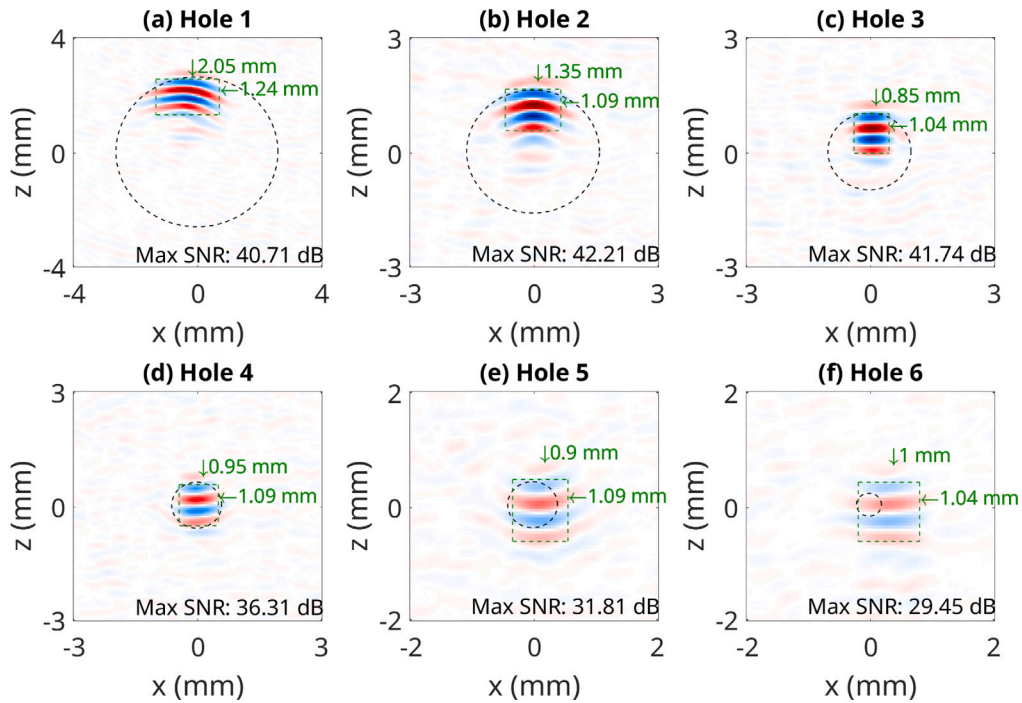


Fig. 22. Zoomed in experimental steel images for each hole within  $K_{V_p}$ .

and  $K'_p$  performing poorly while  $K_{V_p}$  performing the best and  $I_{TFM}$  closely following. A conclusion deriving from this study is that even for data containing increased background “white noise” induced by the transducer,  $K_{V_p}$  will still outperform in comparison to the other techniques with respect to providing a high image SNR.

#### 4.2. Aluminum block defect images

Fig. 27 presents ARTM and TFM-generated images from ultrasound data from the aluminum block with holes in the “AOS” pattern. Five images were generated from ultrasound data acquired from the physical system. Comparisons are made based on (1) identification of all holes

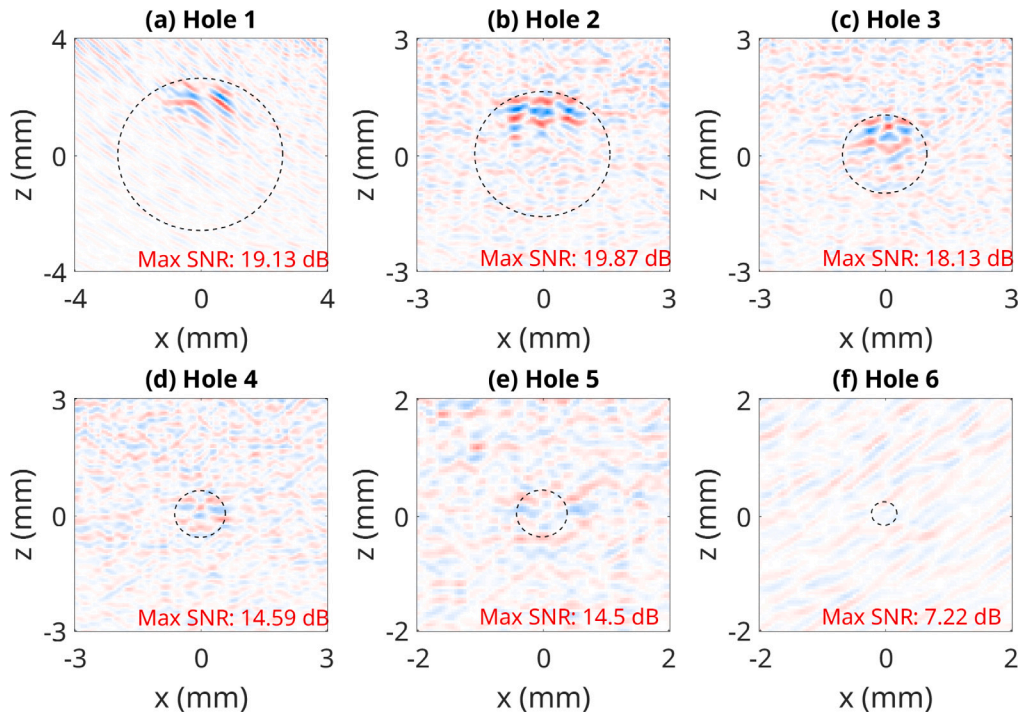


Fig. 23. Zoomed in experimental steel images for each hole within:  $K_y$ .

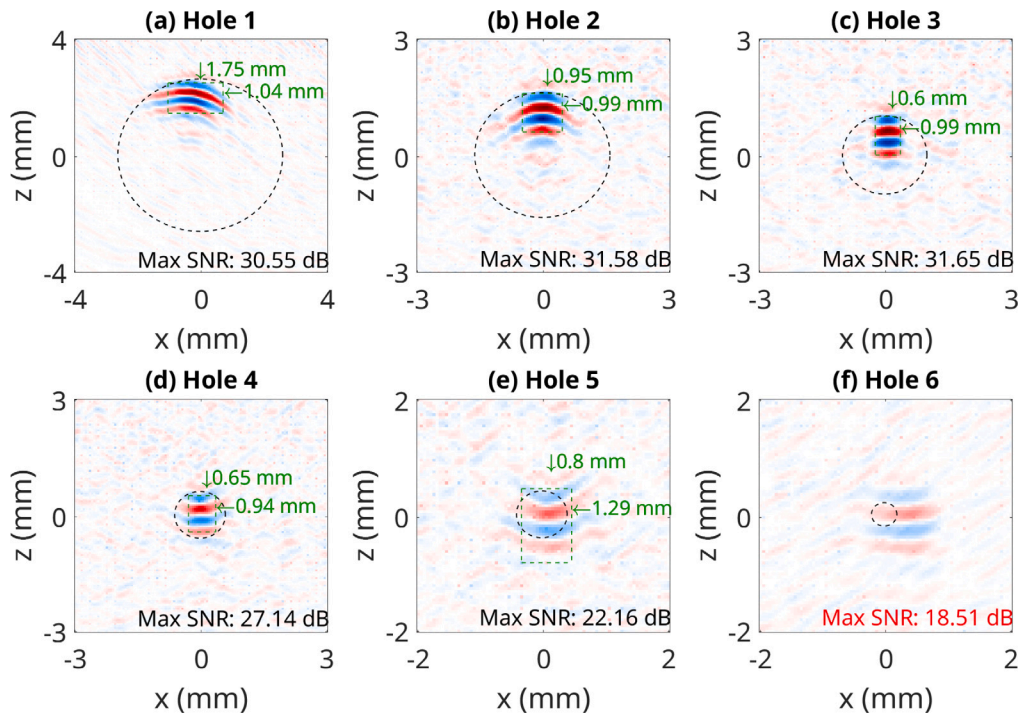


Fig. 24. Zoomed in experimental steel images for each hole within:  $K_p$ .

and (2) average background noise in the domain (artifacts). All holes can be readily identified in Figs. 27(a) and 27(c)–(e), even those located deeper in the domain and obscured by overlying holes. Fig. 27(b) produces an image containing a very faint indication of the deeper defects. For this domain, there is a low-amplitude artifact near the transducer surface present in all images aside from Fig. 27(a). This artifact, though, does not hinder defect identification. In terms of accurately sizing the holes, from visual inspection, it can be seen that Fig. 27(b) provides the most accurate depiction of hole sizes closest to the transducer while

doing a poor job for the deepest defects. The other kernels (Figs. 27(a) and 27(c)–(d)) provide a similar sizing for the uppermost holes, while the TFM image (Fig. 27(e)) more significantly overestimates the largest holes, in addition to obscuring artifacts presence around the first two lines of holes. In contrast to the findings from [24], Fig. 27(d) does not possess artifact cancellation properties; a potential explanation could be that the primary kernels here have fewer opposing artifacts to cancel out through superposition when evaluating the impedance kernel. This could be caused by the results shown in Figs. 27(b) and 27(c) contain

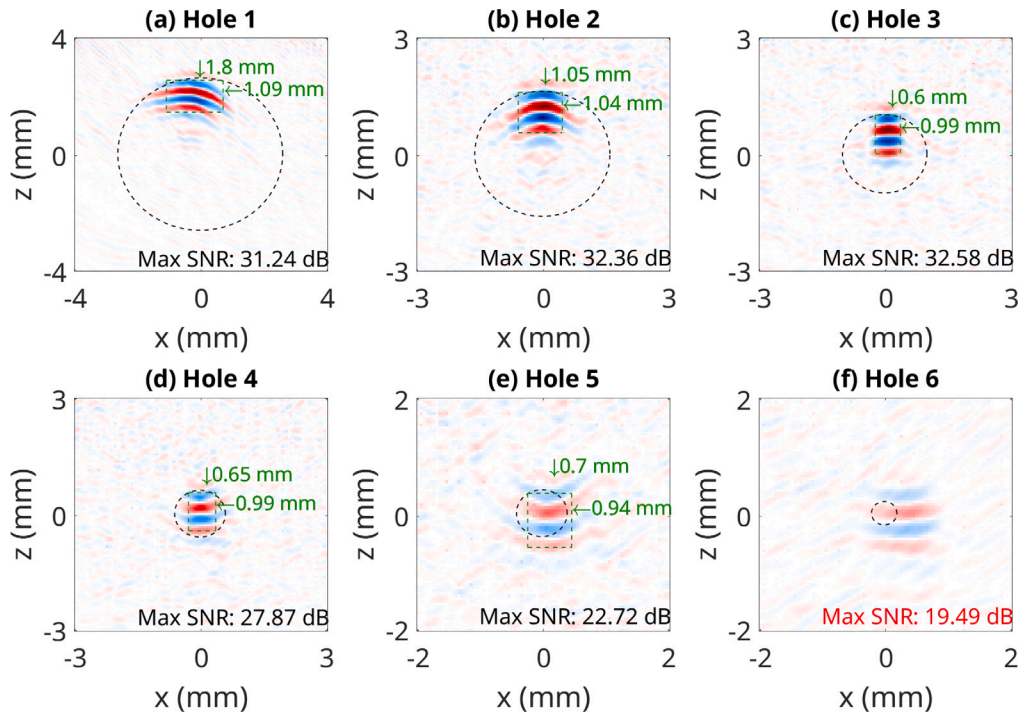


Fig. 25. Zoomed in experimental steel images for each hole within:  $K'_p$ .

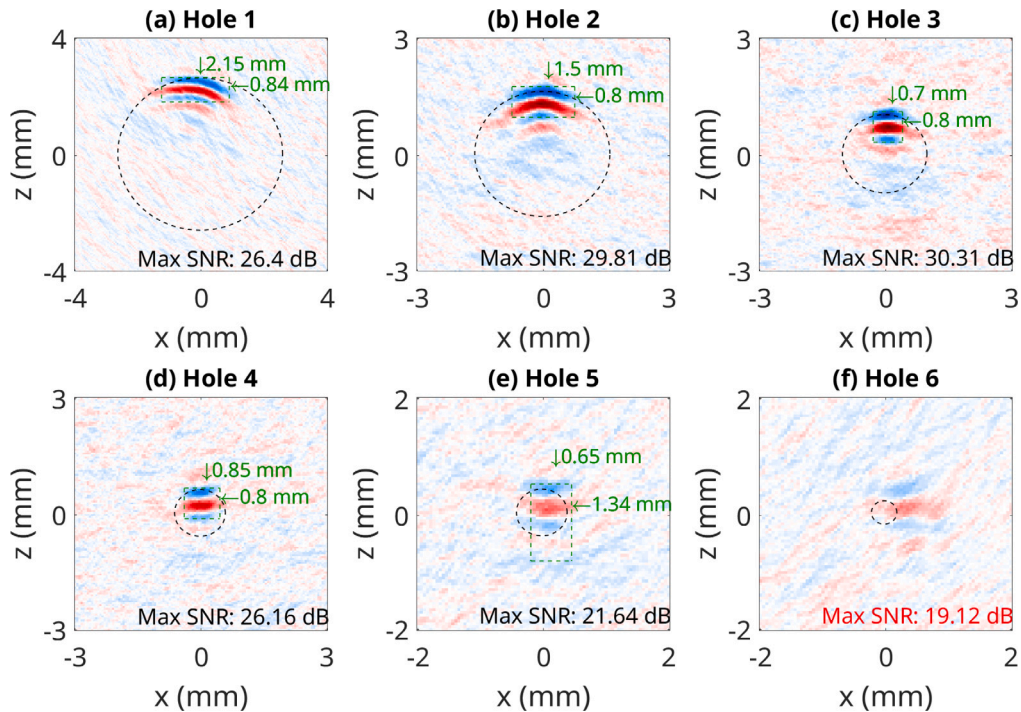


Fig. 26. Zoomed in experimental steel images for each hole within:  $I_{TFM}$ .

additive artifacts, whereas Fig. 27(a) has very few. In addition, the fact that the modeled domain is a simple region with a single wave speed set and density may be a contributing factor as well.

A comparative metric of the total noise is the SNR of the aluminum block images (Fig. 27). The results are presented in Table 11. Like the prior three cases,  $K_{V_p}$  is the superior image in terms of the least average background noise. The significance of this is that, overall,  $K_{V_p}$  will produce the least amount of potentially obscuring artifacts in

comparison to the presented alternatives in a model setup similar to the one shown: a background with a single density and wave speed set and absorbing boundary conditions. Notably, all the other kernels except for  $K_{V_s}$  exceed  $I_{TFM}$  in this regard as well.

The time required to generate images is presented for the aluminum block case as well. The hardware setup is the same. The TFM algorithm only required about 4.07 s per source, while the ARTM algorithm required approximately 1067 s per source. The required computation time

**Table 9**  
Location and sizing comparisons for “Noisy” experimental steel images.

| Hole:     | 1     |        |       | 2     |        |       | 3     |        |       |
|-----------|-------|--------|-------|-------|--------|-------|-------|--------|-------|
| Quantity: | Width | Height | Depth | Width | Height | Depth | Width | Height | Depth |
| $K_{V_p}$ | 2.05  | 1.24   | 13.39 | 1.35  | 1.09   | 14.29 | 0.85  | 1.04   | 14.94 |
| $K_{V_s}$ | ND    | ND     | ND    | ND    | ND     | ND    | ND    | ND     | ND    |
| $K_p$     | 1.75  | 1.04   | 13.44 | 0.95  | 0.99   | 14.34 | 0.60  | 0.99   | 14.94 |
| $K'_p$    | 1.80  | 1.09   | 13.39 | 1.05  | 1.04   | 14.34 | 0.60  | 0.99   | 14.94 |
| $I_{TFM}$ | 2.15  | 0.84   | 13.29 | 1.50  | 0.80   | 14.19 | 0.70  | 0.80   | 14.84 |
| Measured  | 5.2   | 5.2    | 13.3  | 3.2   | 3.2    | 14.3  | 2.0   | 2.0    | 14.9  |
| Hole:     | 4     |        |       | 5     |        |       | 6     |        |       |
| Quantity: | Width | Height | Depth | Width | Height | Depth | Width | Height | Depth |
| $K_{V_p}$ | 0.95  | 1.09   | 15.38 | 0.90  | 1.09   | 15.49 | 1.00  | 1.04   | 15.54 |
| $K_{V_s}$ | ND    | ND     | ND    | ND    | ND     | ND    | ND    | ND     | ND    |
| $K_p$     | 0.65  | 0.94   | 15.43 | 0.80  | 1.29   | 15.49 | ND    | ND     | ND    |
| $K'_p$    | 0.65  | 0.99   | 15.38 | 0.70  | 0.94   | 15.59 | ND    | ND     | ND    |
| $I_{TFM}$ | 0.85  | 0.80   | 15.29 | 0.65  | 1.34   | 15.44 | ND    | ND     | ND    |
| Measured  | 1.2   | 1.2    | 15.3  | 0.8   | 0.8    | 15.5  | 0.4   | 0.4    | 15.7  |

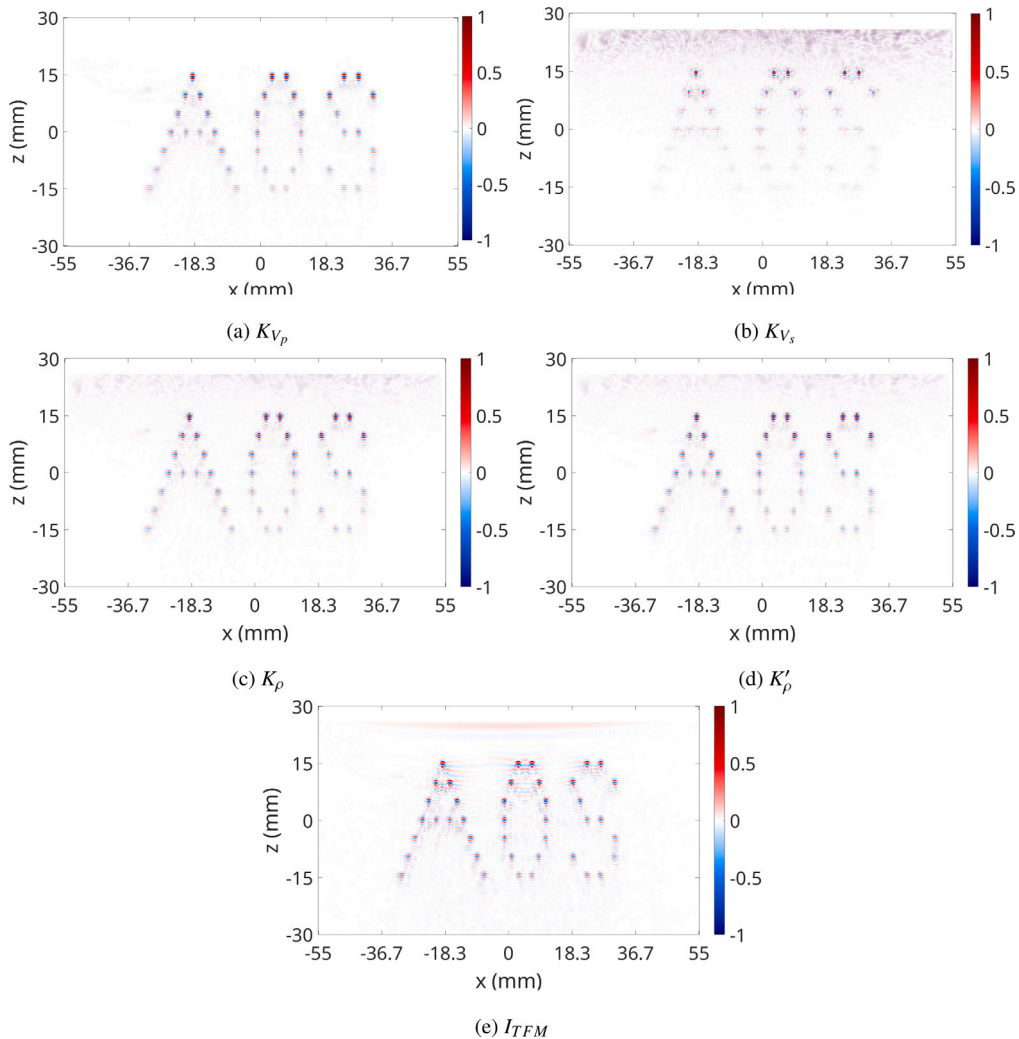


**Fig. 27.** ARTM results for aluminum data with sensitivity kernels: (a)  $K_{V_p}$ , (b)  $K_{V_s}$ , (c)  $K_p$ , and (d)  $K'_p$ . (e) TFM image.

is consistent with the steel block case, with ARTM taking significantly longer to produce images than the TFM algorithm with a homogeneous background. The required computation time for the aluminum block

is longer, as expected for ARTM in this case than it was previously. This is caused by the significant increase in time length for wavefield modeling.

**Table 10**

Maximum signal to noise ratio of “noisy” experimental steel block images.

| Imaging Method | SNR (dB) |
|----------------|----------|
| $K_p$          | 32.09    |
| $K_{V_p}$      | 42.73    |
| $K_{V_s}$      | 22.36    |
| $K'_p$         | 32.97    |
| $I_{TFM}$      | 30.36    |

**Table 11**

Maximum SNR of aluminum block experiment images.

| Imaging Method | SNR (dB) |
|----------------|----------|
| $K_p$          | 40.77    |
| $K_{V_p}$      | 46.10    |
| $K_{V_s}$      | 36.97    |
| $K'_p$         | 41.26    |
| $I_{TFM}$      | 37.39    |

## 5. Conclusion

The ARTM method was implemented to generate phased-array ultrasound images using four imaging kernels:  $K_{V_p}$ ,  $K_{V_s}$ ,  $K_p$  and  $K'_p$ . As a metric of comparison, a TFM-generated phased-array ultrasound image ( $I_{TFM}$ ) is presented as a baseline. This was performed in four different sets of ultrasound data: (1) a numerical representation of a steel block, (2) the corresponding experimental data, (3) the same artificial data with a higher level of noise, and (4) experimental data acquired from an aluminum block, each with side-drilled holes acting as defects. Conclusions for the performance of each imaging method may be extrapolated from the sizing and depth metrics for the steel block studies.  $K_{V_p}$  was demonstrated to be a robust imaging condition that performed well for all three datasets. The only downside to implementing  $K_{V_p}$  was that it performed lowest at characterizing small hole sizes, yet it had the best SNR of the smallest hole in the “noisy” dataset, suggesting that the addition of noise may make other methods difficult to characterize the hole, while  $K_{V_p}$  may be able to still provide an estimate. Repeatedly in each study, imaging conditions based upon  $K_p$  and  $K'_p$  will outperform the others in characterizing the smaller defects unless the level of noise is sufficiently large for it to become difficult to discern the defect edge from the background. Datasets with large amounts of noise will have the best SNR using  $K_{V_p}$ , and accurate defect sizes may be able to be extrapolated if there is both good coverage and the defect is large enough.  $K_{V_s}$  showed promising resolution and size characterization for hole contour for holes centrally located under the phased array in the numerical steel study, and performed worse for holes away from the center of the phased-array. In the experimental datasets,  $K_{V_s}$  had the largest deviation in performance in comparison to the numerical dataset.  $I_{TFM}$  performed middling in each study, having one case where it performed best or often second to third best. A notable advantage in  $I_{TFM}$  in comparison to ARTM images is reduced computational complexity. However, the authors speculate that a more complex domain would allow the benefits of using a wave-equation simulator to become more evident in comparison to the simple delay-and-sum implementation, which is a potential direction for future work.

## CRediT authorship contribution statement

**John D. Day:** Writing – review & editing, Writing – original draft, Visualization, Validation, Formal analysis, Investigation, Methodology. **Jiaze He:** Methodology, Funding acquisition, Conceptualization, Project administration. **Jeffrey Shragge:** Writing – review & editing, Methodology, Conceptualization, Formal analysis. **Paul Sava:** Methodology. **Erin L. Lanigan:** Resources. **Gavin Dao:** Data curation. **Weihua Su:** Writing – review & editing, Resources, Supervision.

## Declaration of competing interest

The authors declare that they have no known competing financial interests or personal relationships that could have appeared to influence the work reported in this paper.

## Acknowledgments

This work was supported by the NASA CAN grant, United States (Grant No. 80NSSC22M0050), which is acknowledged by the authors. The authors would like to thank Delphine Duquette for the contributions during the project.

## Data availability

Data will be made available on request.

## References

- [1] Abhishek S. Quantitative ultrasonic characterisation of surface-breaking cracks (Ph.D. thesis), Nanyang Technological University; 2021.
- [2] Hsu D. Non-destructive evaluation (NDE) of aerospace composites: ultrasonic techniques. In: Non-destructive evaluation (NDE) of polymer matrix composites. Elsevier; 2013, p. 397–422. <http://dx.doi.org/10.1533/9780857093554.3.397>.
- [3] Habib S, Yousuf WB, Mairaj T, Khalid S. Fatigue Crack Growth prediction on A310 aircraft wing using static analysis. In: 2017 14th international bhurban conference on applied sciences and technology. IBCAST, IEEE; 2017, p. 71–5. <http://dx.doi.org/10.1109/IBCAST.2017.7868038>.
- [4] Kramb V, Frock B, Stubbs D. Defect detection and classification in aerospace materials using phased array ultrasonics. In: E-journal of nondestructive testing. Citeseer; 2004.
- [5] Honarvar F, Varvani-Farahani A. A review of ultrasonic testing applications in additive manufacturing: Defect evaluation, material characterization, and process control. Ultrasonics 2020;108:106227. <http://dx.doi.org/10.1016/j.ultras.2020.106227>.
- [6] Chiao RY, Thomas LJ. Analytic evaluation of sampled aperture ultrasonic imaging techniques for NDE. IEEE Trans Ultrason Ferroelectr Freq Control 1994;41(4):484–93. <http://dx.doi.org/10.1109/58.294109>.
- [7] Drinkwater BW, Wilcox PD. Ultrasonic arrays for non-destructive evaluation: A review. NDT & E Int 2006;39(7):525–41. <http://dx.doi.org/10.1016/j.ndteint.2006.03.006>.
- [8] Holmes C, Drinkwater BW, Wilcox PD. Post-processing of the full matrix of ultrasonic transmit–receive array data for non-destructive evaluation. NDT & E Int 2005;38(8):701–11. <http://dx.doi.org/10.1016/j.ndteint.2005.04.002>.
- [9] Muller A, Robertson-Welsh B, Gaydecki P, Gresil M, Soutis C. Structural health monitoring using lamb wave reflections and total focusing method for image reconstruction. Appl Compos Mater 2017;24:553–73. <http://dx.doi.org/10.1007/s10443-016-9549-5>.
- [10] Carcreff E, Dao G, Braconnier D. Fast total focusing method for ultrasonic imaging. In: AIP conference proceedings. vol. 1706, AIP Publishing; 2016, <http://dx.doi.org/10.1109/ULTSYM.2015.0441>.
- [11] Kerr W, Pierce S, Rowe P. Investigation of synthetic aperture methods in ultrasound surface imaging using elementary surface types. Ultrasonics 2016;72:165–76. <http://dx.doi.org/10.1016/j.ultras.2016.08.007>.
- [12] Ginzel E, Bajgholi M, Guimarães M, Foucher F, Rousseau G, Viens M. Total Focusing Method used for flaw sizing in probability of detection determination. J Nondestruct Test 2022;27(7).
- [13] Carcreff E, Braconnier D. Comparison of conventional technique and migration approach for total focusing. Phys Procedia 2015;70:566–9. <http://dx.doi.org/10.1016/j.phpro.2015.08.022>.
- [14] He H, Sun K, Sun C, He J, Liang E, Liu Q. Suppressing artifacts in the total focusing method using the directivity of laser ultrasound. Photoacoustics 2023;31:100490. <http://dx.doi.org/10.1016/j.pacs.2023.100490>.
- [15] Rao J, Saini A, Yang J, Ratassepp M, Fan Z. Ultrasonic imaging of irregularly shaped notches based on elastic reverse time migration. NDT & E Int 2019;107:102135. <http://dx.doi.org/10.1016/j.ndteint.2019.102135>.
- [16] Müller S, Niederleithinger E, Bohlen T. Reverse time migration: A seismic imaging technique applied to synthetic ultrasonic data. Int J Geophys 2012;2012. <http://dx.doi.org/10.1155/2012/128465>.
- [17] Zhang Y, Gao X, Zhang J, Jiao J. An Ultrasonic Reverse Time Migration Imaging Method Based on Higher-Order Singular Value Decomposition. Sensors 2022;22(7):2534. <http://dx.doi.org/10.3390/s22072534>.
- [18] Liu H, Qi Y, Chen Z, Tong H, Liu C, Zhuang M. Ultrasonic inspection of grouted splice sleeves in precast concrete structures using elastic reverse time migration method. Mech Syst Signal Process 2021;148:107152. <http://dx.doi.org/10.1016/j.jymssp.2020.107152>.

- [19] Kaelin B, Guitton A. Imaging condition for reverse time migration. In: Seg technical program expanded abstracts 2006. Society of Exploration Geophysicists; 2006, p. 2594–8. <http://dx.doi.org/10.1190/1.2370059>.
- [20] Yan J, Sava P. Isotropic angle-domain elastic reverse-time migration. *Geophysics* 2008;73(6):S229–39. <http://dx.doi.org/10.1190/1.2981241>.
- [21] Chattopadhyay S, McMechan GA. Imaging conditions for prestack reverse-time migration. *Geophysics* 2008;73(3):S81–9. <http://dx.doi.org/10.1190/1.2903822>.
- [22] Rao J, Yang J, He J, Huang M, Rank E. Elastic least-squares reverse-time migration with density variation for flaw imaging in heterogeneous structures. *Smart Mater Struct* 2020;29(3):035017. <http://dx.doi.org/10.1088/1361-665X/ab6ba4>.
- [23] Luo Y. *Seismic imaging and inversion based on spectral-element and adjoint methods (Ph.D. thesis), Princeton University; 2012.*
- [24] Luo Y, Tromp J, Denel B, Calandra H. 3D coupled acoustic-elastic migration with topography and bathymetry based on spectral-element and adjoint methods. *Geophysics* 2013;78(4):S193–202. <http://dx.doi.org/10.1190/geo2012-0462.1>.
- [25] Sun R, McMechan GA. Pre-stack reverse-time migration for elastic waves with application to synthetic offset vertical seismic profiles. *Proc IEEE* 1986;74(3):457–65. <http://dx.doi.org/10.1109/PROC.1986.13486>.
- [26] Whitmore N, Crawley S. Applications of RTM inverse scattering imaging conditions. In: SEG international exposition and annual meeting. SEG; 2012, p. SEG–2012. <http://dx.doi.org/10.1190/segam2012-0779.1>.
- [27] Claerbout JF. Toward a unified theory of reflector mapping. *Geophysics* 1971;36(3):467–81. <http://dx.doi.org/10.1190/1.1440185>.
- [28] Chang W-F, McMechan GA. Elastic reverse-time migration. *Geophysics* 1987;52(10):1365–75. <http://dx.doi.org/10.1190/1.1442249>.
- [29] Sun R, McMechan GA. Nonlinear reverse-time inversion of elastic offset vertical seismic profile data. *Geophysics* 1988;53(10):1295–302. <http://dx.doi.org/10.1190/1.1442407>.
- [30] Wang W, McMechan GA. Vector-based elastic reverse time migration. *Geophysics* 2015;80(6):S245–58. <http://dx.doi.org/10.1190/geo2014-0620.1>.
- [31] Tromp J, Komatitsch D, Liu Q. Spectral-element and adjoint methods in seismology. *Commun Comput Phys* 2008;3(1):1–32.
- [32] Rocha D, Tanushev N, Sava P. Isotropic elastic wavefield imaging using the energy norm. *Geophysics* 2016;81(4):S207–19. <http://dx.doi.org/10.1190/geo2015-0487.1>.
- [33] Tromp J, Tape C, Liu Q. Seismic tomography, adjoint methods, time reversal and banana-doughnut kernels. *Geophys J Int* 2005;160(1):195–216. <http://dx.doi.org/10.1111/j.1365-246X.2004.02453.x>.
- [34] Guo P, McMechan GA. Compensating Q effects in viscoelastic media by adjoint-based least-squares reverse time migration. *Geophysics* 2018;83(2):S151–72. <http://dx.doi.org/10.1190/geo2017-0235.1>.
- [35] Chang J, Wang C, Tang Y, Li W. Numerical investigations of ultrasonic reverse time migration for complex cracks near the surface. *IEEE Access* 2022;10:5559–67. <http://dx.doi.org/10.1109/ACCESS.2021.3140119>.
- [36] MatWeb. 2025, The Online Materials Information Resource. MatWeb is a division of Automation Creations, Inc. (ACI) of Blacksburg, Virginia. <https://asm.matweb.com>. (Accessed 23 April 2025).
- [37] Kumar V, Silwal V, Ray S. Simulation of seismic wave propagation using spectral-element method for Uttarakhand Himalayan Region with SPECSEM3D. In: 2nd EAGE/aqua foundation Indian near surface geophysics conference & exhibition. 2023, European Association of Geoscientists & Engineers; 2023, p. 1–5. <http://dx.doi.org/10.1093/gji/ggy546>.
- [38] Seriani G, Priolo E. Spectral element method for acoustic wave simulation in heterogeneous media. *Finite Elem Anal Des* 1994;16(3–4):337–48. <http://dx.doi.org/10.1190/1.1821973>.
- [39] Chow B, Kaneko Y, Tape C, Modrak R, Townend J. An automated workflow for adjoint tomography—waveform misfits and synthetic inversions for the North Island, New Zealand. *Geophys J Int* 2020;223(3):1461–80. <http://dx.doi.org/10.1093/gji/ggaa381>.
- [40] Modrak RT, Borisov D, Lefebvre M, Tromp J. SeisFlows—Flexible waveform inversion software. *Comput Geosci* 2018;115:88–95. <http://dx.doi.org/10.1016/j.cageo.2018.02.004>.
- [41] Xie Z, Komatitsch D, Martin R, Matzen R. Improved forward wave propagation and adjoint-based sensitivity kernel calculations using a numerically stable finite-element PML. *Geophys J Int* 2014;198(3):1714–47. <http://dx.doi.org/10.1093/gji/ggu219>.
- [42] Xie Z, Matzen R, Cristini P, Komatitsch D, Martin R. A perfectly matched layer for fluid-solid problems: Application to ocean-acoustics simulations with solid ocean bottoms. *J Acoust Soc Am* 2016;140(1):165–75. <http://dx.doi.org/10.1121/1.4954736>.
- [43] Zhang H, Liu Y, Fan G, Zhang H, Zhu W, Zhu Q. Sparse-TFM imaging of lamb waves for the near-distance defects in plate-like structures. *Metals* 2019;9(5):503. <http://dx.doi.org/10.3390/met9050503>.